PHYSICAL REVIEW E **97**, 033112 (2018)

Electrohydrodynamic coalescence of droplets using an embedded potential flow model

M. Garzon,[1,*] L. J. Gray,[2] and J. A. Sethian[3]
[1] *Department of Applied Mathematics, University of Oviedo, Oviedo, Asturias, Spain*
[2] *119 Berwick Drive, Oak Ridge, Tennessee 37830, USA*
[3] *Department of Mathematics, UC Berkeley and Mathematics Department,*
Lawrence Berkeley National Laboratory, Berkeley, California 94720, USA

(Received 9 March 2017; published 30 March 2018)

The coalescence, and subsequent satellite formation, of two inviscid droplets is studied numerically. The initial drops are taken to be of equal and different sizes, and simulations have been carried out with and without the presence of an electrical field. The main computational challenge is the tracking of a free surface that changes topology. Coupling level set and boundary integral methods with an embedded potential flow model, we seamlessly compute through these singular events. As a consequence, the various coalescence modes that appear depending upon the relative ratio of the parent droplets can be studied. Computations of first stage pinch-off, second stage pinch-off, and complete engulfment are analyzed and compared to recent numerical studies and laboratory experiments. Specifically, we study the evolution of bridge radii and the related scaling laws, the minimum drop radii evolution from coalescence to satellite pinch-off, satellite sizes, and the upward stretching of the near cylindrical protrusion at the droplet top. Clear evidence of partial coalescence self-similarity is presented for parent droplet ratios between 1.66 and 4. This has been possible due to the fact that computational initial conditions only depend upon the mother droplet size, in contrast with laboratory experiments where the difficulty in establishing the same initial physical configuration is well known. The presence of electric forces changes the coalescence patterns, and it is possible to control the satellite droplet size by tuning the electrical field intensity. All of the numerical results are in very good agreement with recent laboratory experiments for water droplet coalescence.

DOI: 10.1103/PhysRevE.97.033112

I. MOTIVATION AND OVERVIEW

Coalescence between liquid surfaces remains a subject of intense research due to its importance in various applications, e.g., emulsion evolution, rain formation in clouds [1], industrial spray painting [2], electrified jets and drops [3,4], particle removal from droplets [5], etc.

Numerically modeling the coalescence of two equal droplets must initially overcome a singular event at the contact point, immediately followed by the formation and expansion of a thin liquid bridge. The evolution of this connecting bridge has been extensively studied, particularly when two drops merge in vacuum or air [6–13]. In this situation, no daughter satellite is ejected from the combined droplet. However, in the coalescence of a drop with a flat liquid surface, a satellite pinches-off from the top in the well known coalescence cascade [13–17].

Recent laboratory experiments by Zhang *et al.* [18] reveal novel pinch-off dynamics and satellite formation during coalescence of unequal size drops, the behavior depending upon the relative sizes of the initial parent droplets and the Ohnesorge number. They found that the critical parent ratio is as small as 1.55 but grows monotonically with the Ohnesorge number and the satellite daughter size is typically about 50% of the mother droplet size. From a computational point of view the replication of these experimental results is very challenging due to the singular events of merging and splitting of fluid interfaces.

Although many experiments and some numerical computations of coalescence assume a viscous fluid model, herein we focus on the nonviscous irrotational flow of two droplets joining and pinching inside a dynamically inactive exterior fluid. In addition, for the droplet length scales reported in the previously mentioned experiments [18], gravity forces are negligible compared to surface tension forces. Gravity is therefore omitted from the model.

Most of the numerical studies of drop coalescence assume that a tiny liquid bridge already exists at $t = 0$ [7,16], thus altering the onset of the merging process and possibly the scaling laws of the neck radii $r(t)$ at early evolution times. Paulsen *et al.* [10] found that all their experimental data for salt water drops are consistent with $r(t) \approx t$ at early times, regardless of the viscosity of the outer fluid. They verified that the dynamics is dominated by the inner fluid despite the much more viscous surroundings.

In previous potential flow computations based upon level set embedding techniques [19–23], a complete Eulerian formulation of the classical Lagrangian equations was developed. The potential flow equations were solved using a boundary integral formulation, with level set numerical schemes employed for surface evolution. This approach has proved to be very robust for simulating various fluid splitting applications, specifically wave overturning and breaking [19], the Rayleigh-Taylor instability of a fluid jet [20], droplet and bubble evolution in a two fluid system [21,22], and electrical droplet deformation [23]. This algorithm assumes an axisymmetric geometry and an explicit sharp interface, requiring the nodal representation of the free surface at each time step. More recently, a complete

---

[*] maria.garzon.martin@gmail.com

three-dimensional algorithm coupling of level sets with Nitsche finite element method has been developed. In this case, the free surface is represented implicitly and only locally recovered at discrete times [24].

For the coalescence studies, an optimal resolution of the free boundary is needed and axisymmetric geometries apply, and the model and algorithm discussed in [20,23] will be employed. Only a brief review will be presented, as complete details can be found in the above mentioned references. It should be noted that, opposed to the current trends to use high order polynomial approximations, sophisticated discontinuous Galerkin methods, and complicated element bases, the numerical schemes herein are classical and first order. Nevertheless, they have proved to be robust in handling singular merging events, as well as previous fluid breaking. The first difficulty in the study of coalescence is to overcome the initial singularity at $t = 0$. Experimental works [10,13] report problems in obtaining reliable data at very early times, while in [7,12,16] computations are initiated with an already existing small bridge. In [8] the formation and growth of initial toroidal bubbles made computations nonviable. In contrast, we are able to initiate the simulations with two spheres touching tangentially at one point, and can therefore study the evolution of the bridge radii at early times. Moreover, many other flow characteristics before and after daughter pinch-off can be investigated. The most significant results obtained from the range of numerical simulations reported are the following.

(i) A detailed classification of coalescence patterns for inviscid liquid droplets.

(ii) The confirmation of self-similar partial coalescence for parent size ratios between 1.6 and 4.

(iii) The possibility of satellite size control by means of electric forces.

This paper is organized as follows. Section II provides a brief review of the physical assumptions and the mathematical model, while Sec. III gives a general overview of the numerical approximation. Section IV is devoted to the numerical simulations of two drops coalescing, starting with equal or unequal sized drops. In the case of two equal droplets we analyze the very early onset of coalescence, as well as the subsequent evolution and self-similar scaling laws of the bridge neck radius and bridge axial length. A comparison of the findings with previous theoretical and experimental published results is presented. To analyze the dynamics of two unequal droplets coalescing, a number of numerical simulations are carried out, from which we are able to classify the various coalescence patterns and satellite radii as a function of parent size ratio. Evidence of self-similar behavior for partial coalescence is also given. Finally, Sec. V investigates the impact of a uniform electric field on satellite pinch-off dynamics.

II. CLASSICAL AND EXTENDED POTENTIAL FLOW MODEL

We briefly introduce the model equations as a detailed presentation can be found in [23]. Let $\Omega_1(t)$ be a three-dimensional fluid (3D) domain immersed in an infinite exterior fluid $\Omega_2(t)$, $\Gamma(t)$ a parametrization of the free surface between both domains at time $t \in [0,T]$, and $\mathbf{R}(\mathbf{s},t)$, $\mathbf{s} = (s_1,s_2)$ the position vector of a fluid particle on the moving front. See Fig. 1 for a 3D sketch of the physical domain. The fluid occupying $\Omega_1(t)$ is considered incompressible, irrotational, and inviscid and the fluid in $\Omega_2(t)$ is dynamically at rest; thus the classical potential Eulerian-Lagrangian formulation reads

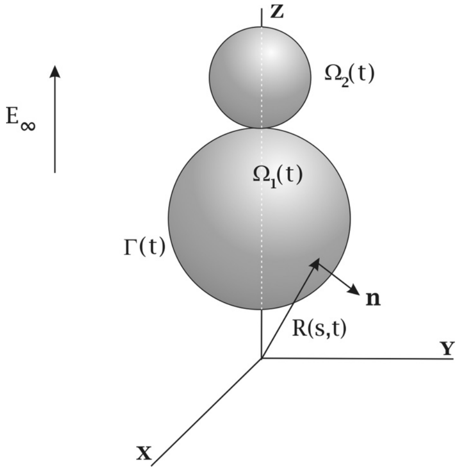

FIG. 1. Three-dimensional sketch of the physical domain. The interior domain consisting of the two touching droplets is $\Omega_1(t)$, $\Omega_2(t)$ is the infinite exterior domain, and $\Gamma(t)$ is the free surface that separates them. The outward normal vector to the free surface is $\mathbf{n}$, $\mathbf{R}(\mathbf{s},t)$ is the position vector of a fluid particle on the front, and E_∞ is the far field electric field intensity.

$$\mathbf{u} = -\nabla\phi \quad \text{in } \Omega_1(t), \tag{1}$$

$$\Delta\phi = 0 \quad \text{in } \Omega_1(t), \tag{2}$$

$$\frac{\partial \mathbf{R}}{\partial t} = \mathbf{u} \quad \text{on } \Gamma(t), \tag{3}$$

$$D_t\phi = f \quad \text{on } \Gamma(t), \tag{4}$$

where $\mathbf{u} = \mathbf{u}(x,y,z,t)$ is the velocity field, $\phi = \phi(x,y,z,t)$ is the velocity potential, and D_t stands for the convective derivative, $D_t\phi = \frac{\partial\phi}{\partial t} + \mathbf{u}\cdot\nabla\phi$. The function $f = f(x,y,z,t)$ contains the contribution of the various forces acting on $\Gamma(t)$.

To include electrical forces on the dynamics, we assume that the fluid in $\Omega_2(t)$ is an insulator gas (or liquid) of permittivity ϵ. In response to an electric field $\mathbf{E} = \mathbf{E}(x,y,z,t)$ applied to the system, the electric charges in $\Omega_2(t)$ do not flow but polarize, creating electric stresses acting on the liquid surface. The fluid in $\Omega_1(t)$ is considered a perfect conductor and charges flow instantaneously from the liquid bulk to the surface. The electric field is thus $\mathbf{E} = \mathbf{0}$ inside $\Omega_1(t)$, $\Gamma(t)$ is an electric equipotential surface, and, as the exterior domain is unbounded, we set $\mathbf{E}$ to be uniform and parallel to the symmetry axis at the far field. Under these assumptions, $\mathbf{E}$ is solenoidal and can be expressed as the gradient of an electric potential field $U = U(x,y,z,t)$:

$$\mathbf{E} = -\nabla U \quad \text{in } \Omega_2(t), \tag{5}$$

$$\Delta U = 0 \quad \text{in } \Omega_2(t), \tag{6}$$

$$U = U_0(t) \quad \text{on } \Gamma(t), \tag{7}$$

$$U = -E_\infty z \quad \text{at infinity.} \tag{8}$$

Here E_∞ is the electric field intensity at the far field. In the present application we consider that the flow is driven by inertia, surface tension, and electric stresses; therefore, the function f in Eq. (4) is

$$f = \frac{1}{2}|\mathbf{u}|^2 - \frac{1}{\rho}\left(\gamma\kappa - \frac{\epsilon}{2}E_n^2\right), \tag{9}$$

where $E_n = \mathbf{n}\cdot\nabla U$ and $\mathbf{n}$ is the unit normal vector pointing from the interior to the exterior domain. The surface tension contribution is $\gamma\kappa$, where κ is twice the mean curvature of the surface and γ is the surface tension coefficient. Note that gravity forces have been neglected as the bond number is considered to be small, $B_0 \ll 1$. To make the equations dimensionless we introduce a characteristic length scale r_0, capillary time scale $t_0 = (\rho r_0^3/\gamma)^{1/2}$, and electric field intensity scale $E_0 = [2\gamma/(\epsilon r_0)]^{1/2}$. All equations remain unchanged, except f in (4) that becomes

$$f = \tfrac{1}{2}|\mathbf{u}|^2 - \kappa + E_n^2, \tag{10}$$

and E_∞ in (4) is also nondimensional hereafter. To obtain the extended potential flow model, note that Eqs. (3) and (4), which are posed on a moving surface, can be reformulated in a fixed domain using the level set–extended potential technique described in [19,20]. In this approach, the moving front $\Gamma(t)$ and velocity potential $\phi|_{\Gamma(t)}$ are embedded into functions $\Psi = \Psi(x,y,z,t)$ and $G = G(x,y,z,t)$ of one higher dimension, respectively. The level set function Ψ and the extended velocity potential function G are defined on the fixed computational domain Ω_D that contains the free boundary for $t \in [0,T]$ and such that

$$\Psi(\mathbf{R}(\mathbf{s},t),t) = 0, \tag{11}$$

$$G(\mathbf{R}(\mathbf{s},t),t) = \phi|_{\Gamma(t)} \tag{12}$$

for $t \in [0,T]$. Following the derivation in [20], Eqs. (3) and (4) transform into

$$\Psi_t + \mathbf{u}_{\text{ext}}\cdot\nabla\Psi = 0 \quad \text{in } \Omega_D, \tag{13}$$

$$G_t + \mathbf{u}_{\text{ext}}\cdot\nabla G = f_{\text{ext}} \quad \text{in } \Omega_D, \tag{14}$$

respectively. The subscript "ext" in Eqs. (13) and (14) denotes the extension of f and $\mathbf{u}$ on the free boundary onto Ω_D. These extensions are performed such that the level sets of each velocity component are orthogonal to the level sets of Ψ; see [25,26].

The level set–extended potential flow model, see [20,21], coupled with the electrical problem in $\Omega_2(t)$ may be written as

$$\mathbf{u} = -\nabla\phi \quad \text{in } \Omega_1(t), \tag{15}$$

$$\Delta\phi = 0 \quad \text{in } \Omega_1(t), \tag{16}$$

$$\phi = G \quad \text{on } \Gamma(t), \tag{17}$$

$$\Psi_t + \mathbf{u}_{\text{ext}}\cdot\nabla\Psi = 0 \quad \text{in } \Omega_D, \tag{18}$$

$$G_t + \mathbf{u}_{\text{ext}}\cdot\nabla G = f_{\text{ext}} \quad \text{in } \Omega_D, \tag{19}$$

$$\mathbf{E} = -\nabla U \quad \text{in } \Omega_2(t), \tag{20}$$

$$\Delta U = 0 \quad \text{in } \Omega_2(t), \tag{21}$$

$$U = U_0(t) \quad \text{on } \Gamma(t), \tag{22}$$

$$U = -E_\infty z \quad \text{at infinity}. \tag{23}$$

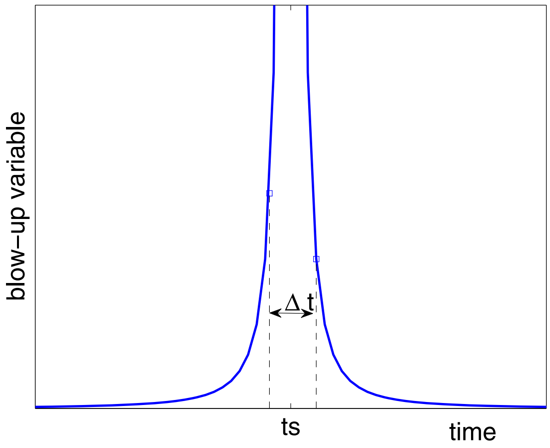

FIG. 2. Time stepping provides a regularization of blow-up variables at singular time $t = t_s$.

The boundary conditions for Eqs. (18) and (19) can be set to $\mathbf{n}_D\cdot\nabla\Psi = 0$ and $\mathbf{n}_D\cdot\nabla G = 0$, respectively, on $\partial\Omega_D$, $\mathbf{n}_D$ denoting the exterior normal to $\partial\Omega_D$. These assumptions mean that the level sets of Ψ and G will intersect $\partial\Omega_D$ orthogonally.

Let t_ϵ be an infinitesimal number and t_s the time at which a flow singularity occurs, i.e., break-up or merging. It has been numerically demonstrated [20] that away from $t \in [t_s - t_\epsilon, t_s + t_\epsilon]$ the level set–extended potential flow model, Eqs. (15) to (19), is equivalent to the classical potential flow Eulerian-Lagrangian formulation. For practical purposes it makes sense to set t_ϵ as the time at which the inviscid

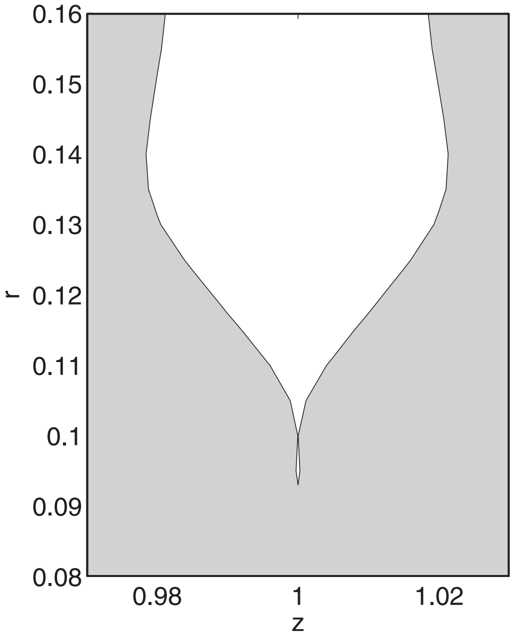

FIG. 3. Initial stage evolution: reconnection event at $t = 0.00155$.

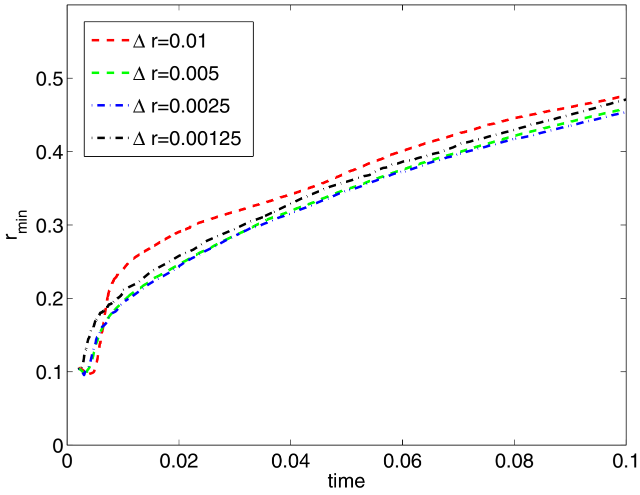

FIG. 4. Minimum neck radius evolution for the various grids.

assumptions are no longer valid, which happens at length scales of a few nanometers.

Equations (15) to (19) are used for pure hydrodynamics one fluid problems such as droplet coalescence by surface tension, whereas the system (15) to (23) has to be considered to model electrohydrodynamic droplet coalescence.

We conclude this section with a brief discussion of the physical assumptions introduced in the computational model. Concerning the perfect conductor assumption, the characteristic electrical relaxation time is $t_e = \epsilon_l / K_l$, where K_l and ϵ_l are the electrical conductivity and permittivity of the liquid, which makes $t_e = 3.5\times 10^{-6}$ s for methanol and $t_e = 4.74\times 10^{-8}$ s for water. As t_e is the time required for the surface charge to approach its equilibrium value, in physical settings when this is much less than the capillary time scale, t_0, $t_e \ll t_0$, the fluid can be considered as perfectly conducting. As an example, for liquid methanol the capillary time is $t_0 \geqslant 1.74\times 10^{-5}$ s for droplet radius $r_0 \geqslant 20\ \mu\text{m}$, whereas for water droplets, $t_0 \geqslant 1.17\times 10^{-7}$ s for $r_0 \geqslant 1\ \mu\text{m}$. Therefore, the limiting drop size for these two liquids can be set to $r_0 = 20\ \mu\text{m}$ and $r_0 = 1\ \mu\text{m}$, respectively. Finally, for liquids such as water, methanol, or air, the inviscid flow assumption holds for length scales above a few nanometers.

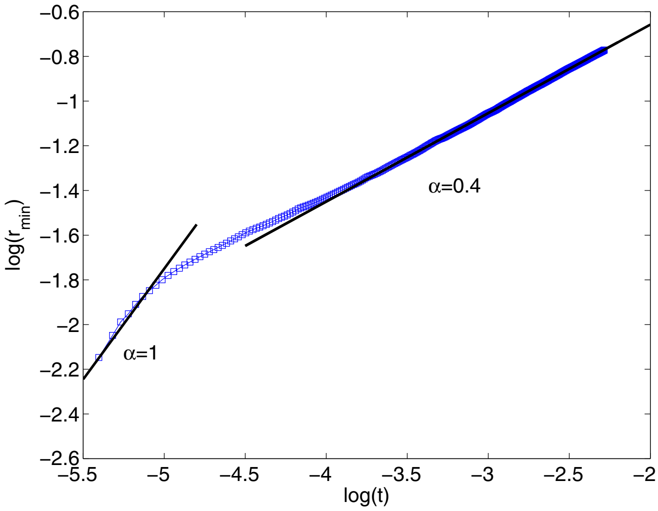

FIG. 5. Log-log plot of minimum neck radius evolution for two equal droplets coalescing. Base-e logarithms.

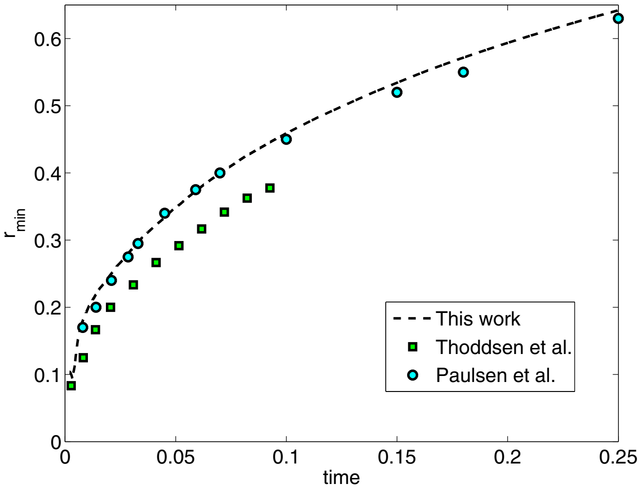

FIG. 6. Comparison of the minimum neck radius evolution for two equal droplets coalescing: this work, Thoroddsen *et al.*, and Paulsen *et al.* (The numbers from both authors have been read off from their figures, and therefore they cannot be considered as exact data.)

III. NUMERICAL APPROXIMATION METHODOLOGY

This section provides an overview of the numerical algorithms; a complete description can once again be found in [20,23].

The numerical approximation of the model equations requires the time and space discretization of Eqs. (18) and (19), the algorithm for the Laplace equations, Eqs. (16) and (21), and the coupling procedure between the two solvers. The time discretization is an explicit forward Euler scheme, with time step Δt. At each discrete time t_n, given $\Psi^n = \Psi(t_n)$ and $G^n = G(t_n)$ the following semidiscretized system has to be

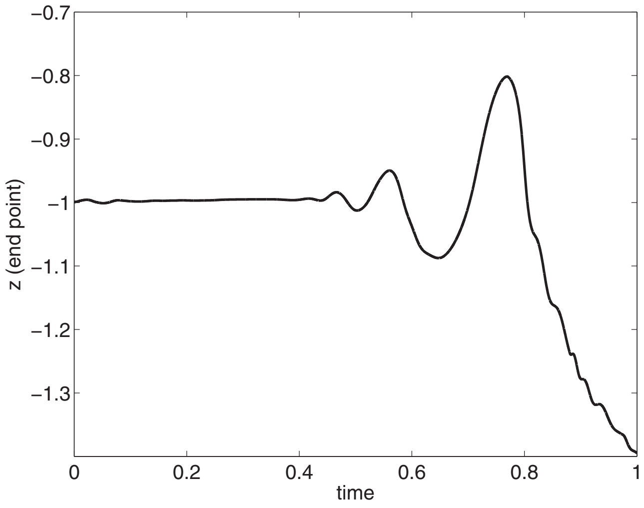

FIG. 7. Left end drop axial coordinate evolution for two equal droplets coalescing.

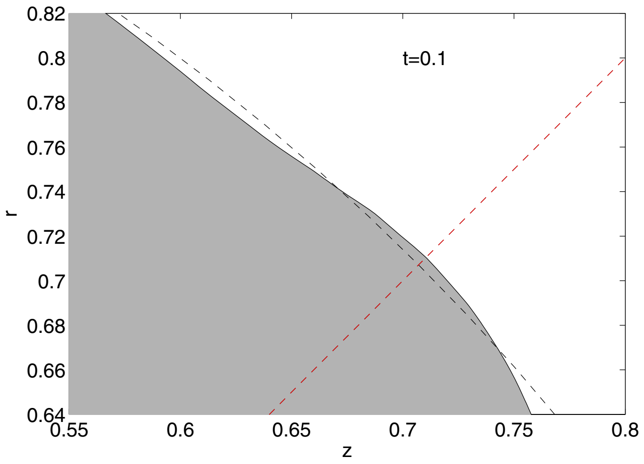

FIG. 8. Capillary wave amplitude. Focused front at $t = 0.1$ and superimposed initial condition at $t = 0$ (dashed). The dashed red line is the line $y = x$.

solved:

$$\mathbf{u}^n = -\nabla\phi^n \quad \text{in } \Omega_1(t_n), \tag{24}$$

$$\Delta\phi^n(x,y,z) = 0 \quad \text{in } \Omega_1(t_n), \tag{25}$$

$$\phi^n|_{\Gamma_{t_n}} = G^n|_{\Gamma_{t_n}}, \tag{26}$$

$$\frac{\Psi^{n+1} - \Psi^n}{\Delta t} = -\mathbf{u}^n_{\text{ext}} \cdot \nabla\Psi^n \quad \text{in } \Omega_D, \tag{27}$$

$$\frac{G^{n+1} - G^n}{\Delta t} = -\mathbf{u}^n_{\text{ext}} \cdot \nabla G^n + f^n_{\text{ext}} \quad \text{in } \Omega_D, \tag{28}$$

$$\mathbf{E}^n = -\nabla U^n \quad \text{in } \Omega_2(t_n), \tag{29}$$

$$\Delta U^n(x,y,z) = 0 \quad \text{in } \Omega_2(t_n) \tag{30}$$

[the boundary conditions for Eq. (30) have been omitted]. For the spatial discretization of Eqs. (27) and (28), a set of points in Ω_D is defined by a Cartesian grid with uniform mesh size h and suitable finite difference level set schemes are applied. In particular, a first order upwind scheme has been used to approximate the convective terms in these two equations.

The solutions of the Laplace equation (25) and (29) are crucial, as they provide the electric stresses on the interface, as well as the velocity to advance the free boundary and the interface boundary condition.

For the axisymmetric geometries encountered herein, a linear element Galerkin boundary integral solution [27] has been employed. This approach works with a sharp (explicit) interface representation and it accommodates the highly nonuniform meshes needed to capture the rupture and merging of fluid domains. Note that Eqs. (24) to (26) and (30) are strongly coupled to Eqs. (27) and (28). First, the Dirichlet boundary condition (26) is obtained from the spatial mesh values of G^n in Ω_D and secondly $\mathbf{u}$ has to be provided from the boundary element calculation to yield $\mathbf{u}^n_{\text{ext}}$. Also $\mathbf{u}$ and $\mathbf{n} \cdot \nabla U$ are needed to obtain f^n_{ext} in the mesh points of Ω_D.

The continuous time interval $[0,T]$ is discretized as $t \in \{t_n,\ n = 1,N\}$ with $\Delta t = t_{n+1} - t_n$ chosen adaptively so that the CFL condition is fulfilled and so that small amplitude capillary waves appearing on the front can be resolved. Specifically, the chosen time step criterion is

$$2t_\epsilon \leqslant \Delta t \leqslant \min\left(\frac{h}{|\mathbf{u}|\text{max}}, 0.2\Delta s^{3/2}_{\text{min}}\right), \tag{31}$$

where, as mentioned above, h is the Ω_D grid spacing, Δs is the free surface node spacing, and $2t_\epsilon$ is a lower bound for the time step.

For an algorithm that aspires to handle topological changes, a primary difficulty is to robustly handle the times immediately before and after a singularity at $t = t_s$. Not only does the

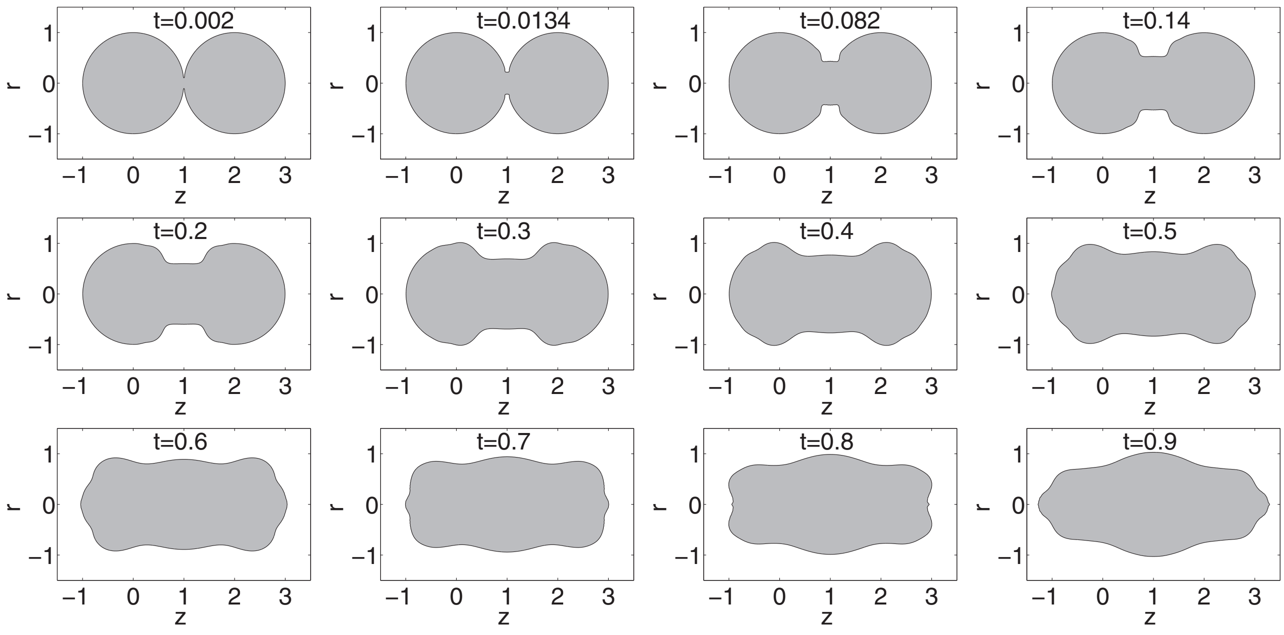

FIG. 9. Fronts of two equal drops coalescing at indicated times. Taking $t_0 = 1720\ \mu$s these dimensionless times correspond to $3.44, 23.05, 141.04, 240.8, 344, 516, 688, 860, 1032, 1204, 1376, 1548\ \mu$s, respectively.

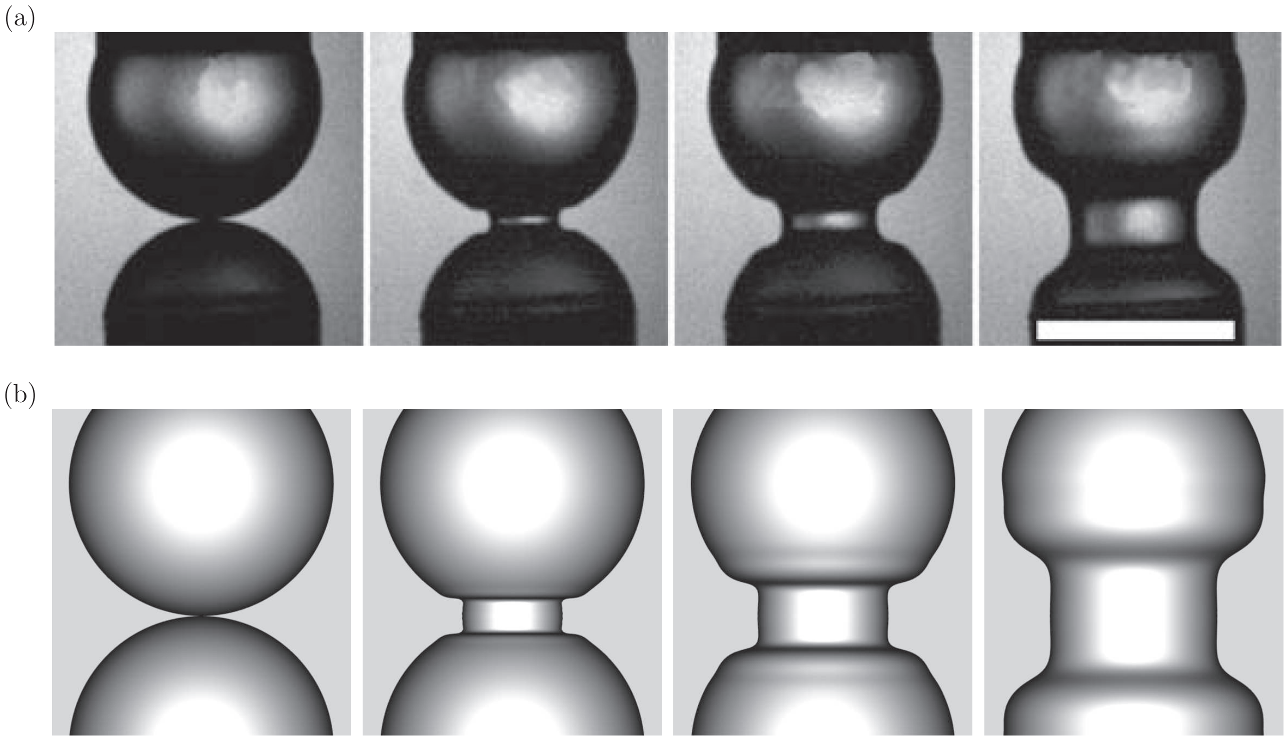

FIG. 10. (a) Laboratory photographs taken from [13]. (b) Computational results for drop shape evolution during coalescence, at real times 0,100,200,400 μs. The top and bottom droplet radii are $R_b = 0.573$ and $R_t = 0.0.597$, and the scale bar is 1 mm long. The nondimensional computation times have been converted using the characteristic time scale $t_0 = 1720$ μs.

domain go through a spatial singularity at $t = t_s$ but the main variables blow up for $t \rightarrow t_s$. In the present approach the topological changes are embedded in the smooth functions Ψ and G. For the function singularities, the time stepping is such that $t_n \neq t_s$ for $n = 1,N$ and the minimum time step $2t_\epsilon$ effects a regularization; see an explanatory sketch in Fig. 2.

It is worth mentioning that the convergence of the algorithm with respect to the mesh parameters has been thoroughly studied in previous works. In [19,20,22], analytical solutions were employed to perform detailed numerical convergence studies, with the errors in the axial and radial velocities and the velocity potential measured in the $L_2(\Gamma(t))$ norm. Conservation of volume and energy were also checked, and the relative errors were always below 1%. The results confirmed the theoretical behavior of first order in time and almost first order in space. Moreover, a comparison of the simulations with existing theoretical self-similar solutions and laboratory

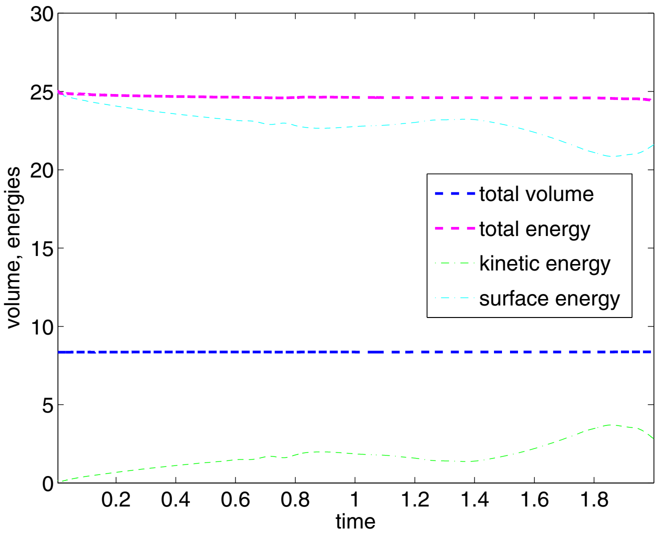

FIG. 11. Total volume and energy evolution; kinetic and surface energies evolution for two equal droplets coalescing. $t = 2$ nondimensional elapsed time.

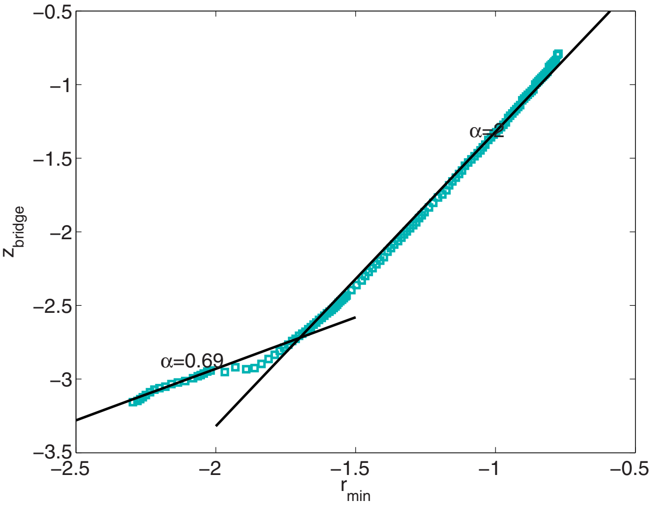

FIG. 12. Log-log plot of bridge height $z_{\rm bridge}(t)$ versus minimum neck radius for two equal droplets coalescing. The more persistent exponent is $\alpha = 2$. Base-e logarithms.

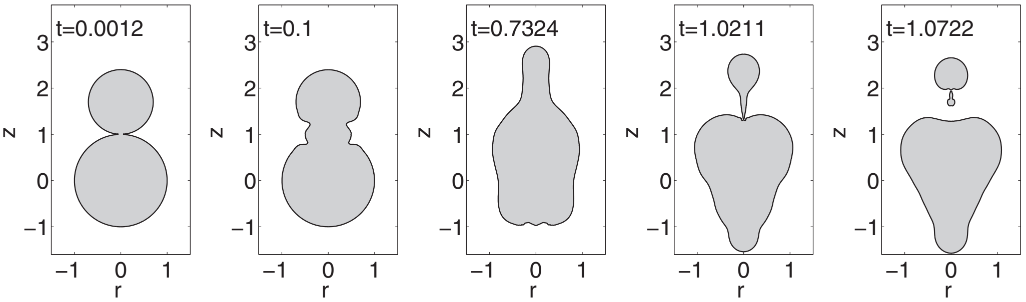

FIG. 13. Several snapshots and partial coalescence pinch-off pattern for $R_m = 0.70$. The tail of the daughter droplet is long enough to generate a visible tertiary droplet.

experiments were also presented in [20,21,23]. The conclusion drawn from these previous works is that this simple algorithm, first order in time and space, is indeed robust enough to handle fluid breakup and reconnections, and gives sufficiently accurate results provided an appropriate mesh resolution is employed.

IV. DROPLET COALESCENCE SIMULATIONS

This section reports on the numerical simulations of the coalescence of two drops. The computations are carried out in the two-dimensional (r,z) plane, with z the symmetry axis; the fixed domain Ω_D, with regular mesh size $h = \Delta r = \Delta z$, is chosen so that it contains the moving boundary for the simulated time span. Comparison with previous computations and laboratory experiments will be presented for both equal and different sized initial drops. For equal sized droplets, the main current controversy is associated with the very early stages of evolution at first contact, from a theoretical, computational and experimental point of view. In the case of droplets of different sizes, recent experiments by Zhang *et al.* [18] have shown a much richer dynamics: after the first coalescence of mother and father droplets, and depending upon the relative sizes of the parents, a daughter droplet may pinch off. Both issues are addressed below.

A. Coalescence of equal size droplets

The coalescence process for two drops of equal size can be summarized as follows. After the first contact they merge by forming a liquid bridge connecting them that grows in time. A capillary wave develops at the contact point and propagates away from the singularity. At early stages of the merging process the drop end points barely move; the dynamics occurs mainly in the bridge zone. At various times the capillary wave reaches the drop ends, causing visible oscillations until the equilibrium state is finally achieved.

For the numerical simulations the initial geometry consists of two spherical droplets with $R = 1$, centered at $z = 0$ and $z = 2$, and thus the initial contact point is at $z = 1$. The fixed domain for the level set computations is $\Omega_D = [-1.5,1.5] \times [-1.5,3.5]$ and the time span considered is $t \in [0,1]$. A good validation of the numerical results is to check for convergence with respect to the discretization parameters. The simulations were therefore run with four different mesh sizes: $\Delta r = \Delta z = 0.01, 0.005, 0.0025, 0.00125$.

For the discretization of the free boundary, a high resolution is clearly needed near the contact point, whereas the surface mesh can be cruder away from this point. To start, $\Delta s = 0.02$ near $z = 1$ and this distance is gradually increased away from the contact point using the regridding technique established in [20]. Over the course of the simulation the number of points N_p representing the free surface varies between $N_p = 141$ and $N_p = 135$. The time step is chosen adaptively according to the criteria given by the formula in (31), leading to time steps as low as $\Delta t = 1.\times 10^{-5}$ in order to accurately resolve for the initial perturbation. Once a steady neck growth is achieved, the time step can be made significantly larger, around $\Delta t = 1.\times 10^{-3}$.

Note that, due to the robustness of the level set method in handling topological changes, the initial coalescence set up is simply two spheres touching tangentially at a single point, without any artificial smoothing (other than that inherent in the discretization procedure). This should be compared with previous methods for dealing with the challenging issue of avoiding the singularity at $t = 0$. The commonly employed method is to assume that immediately after the two free surfaces touch, a small nonzero sized bridge instantaneously appears

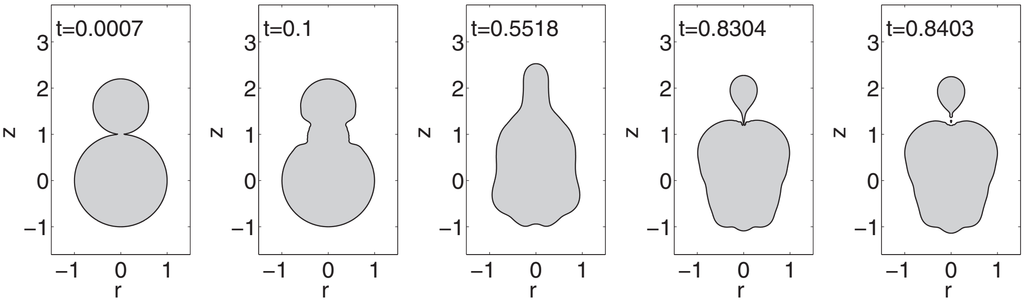

FIG. 14. Several snapshots and partial coalescence pinch-off pattern for $R_m = 0.60$. Here the tertiary droplet is almost nonvisible.

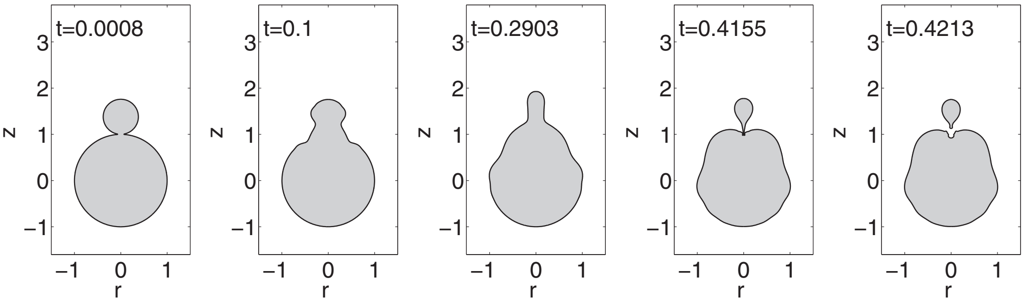

FIG. 15. Several snapshots and partial coalescence pinch-off pattern for $R_m = 0.38$. The pinch-off of the daughter droplet occurs above the top of the father droplet.

[7,8,10,16]. Another recent approach is the so called interface-disappearance model described in [12] that suppresses the initial singularity but involves a much more complex mathematical model and the tuning of various model parameters.

Given the importance of the $t = 0$ algorithm, further details on how the calculation is initiated are provided. Choosing the contact point to be a grid point of Ω_D, the level set function Ψ is initialized as the signed distance function to the front and the zero level set accurately reproduces the circles. The initial velocity potential on the free boundary, namely the two touching spheres, is set to zero. Ideally, with this zero velocity potential the Laplace solver will return vanishing velocity field and there will be no movement. However, round-off errors in the computed velocities, on the order of 10^{-10} to 10^{-6}, initiate the set up of coalescence. However, if exactly zero velocities replace the Laplace solution, it was seen that the level set function remained the same for at least 30 time steps; thus the merging was not forced geometrically by the level set function itself.

There is no claim that the initial contact evolution algorithm is physically correct (whether or not molecular forces play an important role is still a matter of discussion; see [9]). However, provided the spatial-temporal resolution is fine enough to resolve the small scales involved, the initial stages of coalescence qualitatively match with experimental observations. Moreover, by not relying on an artificial bridge, the algorithm is simple and straightforward.

In the present computations the early stages occur in the time interval $t \in [0,0.002]$, where the length of the contact line is stable or even diminishes with time. It is worth reporting that at the times $t = 0.00111$ and $t = 0.00155$ two free boundary reconnections take place. This hypothetically entraps a toroidal bubble of radius 5×10^{-5} nondimensional units; Fig. 3 displays a zoom of the area at $t = 0.00155$. These events are easily handled by the level set technique and the computation proceeds smoothly.

Once the liquid bridge develops between the drops, the evolution of the minimum neck radius $r_{\min}$ is of considerable interest, with theoretical and experimental works indicating the existence of certain scaling laws. Duchemin *et al.* [8] established that, for inviscid fluids, capillary pressure should balance dynamical pressure at early stages of the process,

$$\rho\left(\frac{dr_{\min}}{dt}\right)2 \approx \Delta p,$$

resulting in the scaling law

$$r_{\min} \approx \left(\frac{\gamma R}{\rho}\right)^{1/4} t^{1/2},$$

where again R is the droplet radius.

More recently, Paulsen *et al.* [11] distinguished two different regimes for inviscid drop coalescence: an initial regime (never identified before) that they named the inertial-limited-viscous regime and a pure inertial regime. The scaling laws proposed by these authors are $r_{\min} \approx t$ and the above $r_{\min} \approx t^{1/2}$, respectively. They also conclude that the initial regime should apply for drops of any viscosity.

A basic characterization of the merging process is therefore the time history of the minimum neck radius. In Fig. 4 we plot $r_{\min}$ versus t for the four different mesh sizes, from which we can conclude that the results are, at the present refinement level, independent of the level set discretization. To check the proposed scaling laws, Fig. 5 plots $\log(r_{\min})$ versus $\log(t)$ (here and in what follows, results corresponding to

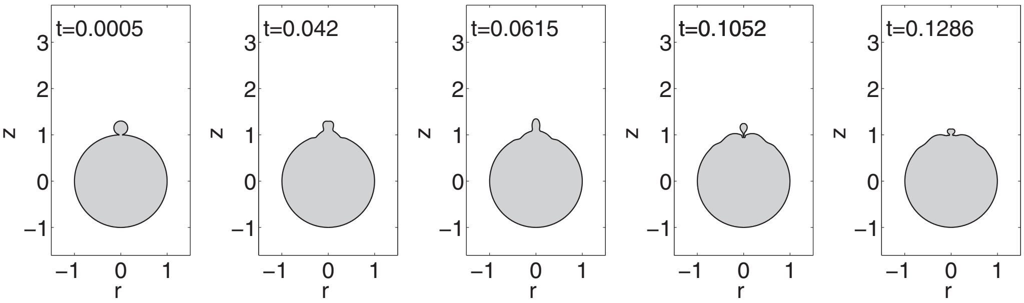

FIG. 16. Several snapshots and partial coalescence pinch-off pattern for $R_m = 0.15$. The pinch-off of the daughter droplet occurs below the top of the father droplet.

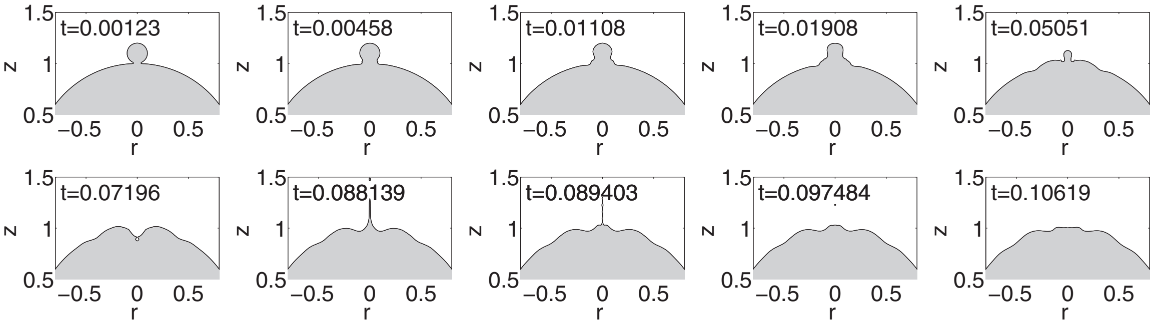

FIG. 17. Fronts of two drops, $R_1 = 1, R_2 = 0.1$, coalescing at indicated times.

$\Delta r = \Delta z = 0.005$ are employed; they provided enough accuracy and reasonable computing time). Clearly, two different regimes can be identified. For very early times, $t \in [0.004,0.007]$, a linear fit performed with Matlab gives an exponent of $\alpha = 1$, while for $t \in [0.018,0.15]$ (and even beyond), a very stable exponent of $\alpha = 0.4$ is obtained. The more persistent exponent of $\alpha = 0.4$ found in this work agrees very well with previously reported experimental results [7,10,13]. Moreover, Fig. 6 provides a comparison between the present numerical simulation and experimental results, namely Fig. 7 in [13], and Fig. 3.*F* of Paulsen *et al.* [11].

To compare not only drop shapes but also time occurrences, a particular laboratory experiment has been chosen, namely the water experiment described by Fig. 12 in [13]. The droplet radii are $r_0 = R = 0.6$ mm (his exact values are $R_b = 0.573$ and $R_t = 0.597$), and the characteristic time scale is then $t_0 = \sqrt{\rho r_0^3/\gamma} = 1720\ \mu$s.

In Fig. 7 the evolution of the left end drop axial coordinate is depicted, the left end referring to the droplet profiles in Fig. 9. As can be observed, droplet deformation for $t \in [0,0.4]$ is very much localized on the bridge region as the end point barely moves. The capillary wave reaches the end point at around $t = 0.5$ and a maximum deformation occurs at $t \approx 0.8$. This corresponds to $t = 1367\ \mu$s, and thus the wave has traveled about 90° from the contact point in 688 μs; this compares well with the experimental time of 800 μs reported in [18]. In Fig. 8 we show the amplitude of the capillary wave with respect to the superimposed initial condition at time $t = 0.1$. We have focused the capillary wave amplitude over the radial direction $y = x$. The amplitude of the wave with respect to the sphere of $R = 1$ is approximately $(4–5)\times 10^{-3}$.

Drop profiles at selected times are depicted in Fig. 9, the symmetry axis being horizontal. For comparison, Fig. 10(a) shows the laboratory profiles taken from [13], while 3D renderings of computed profiles (b) are shown at corresponding times. The conversion from laboratory times 0, 100, 200, and 400 ms to nondimensional times is through the the characteristic time scale $t_0 = 1720\ \mu$s. The evolution of the computed droplet profiles seems to be slightly faster than the experiment, but this is mainly due to the different drawing scales used for the (a) and (b) snapshots. We have continued this simulation until $t = 2$ nondimensional time units to check volume and energy conservation. Figure 11 shows the total volume and energy evolution, as well as the distribution into kinetic and surface energy. The next subsection provides a deeper discussion of the $r_{\min}$ scaling law.

Scaling laws

Self-similar solutions of flows approaching singularities have been extensively studied. Useful scaling laws for the flow variables can be derived theoretically from dimensional analysis and from the balance of forces driving and opposing fluid motion. These results can be checked with, and provide validation for, numerical simulations.

For fluid breakup there is a well-established agreement (theory, simulations, and experiments) that the solution in the pinch-off region is self-similar as $\tau = t_p - t \ \to 0$ [20,21]. Here τ is the time remaining to pinch-off time, t_p; see [28].

For coalescence, however, there is no general concensus at this point, and thus an area of current research. The variables most frequently studied are the radius and axial length of the

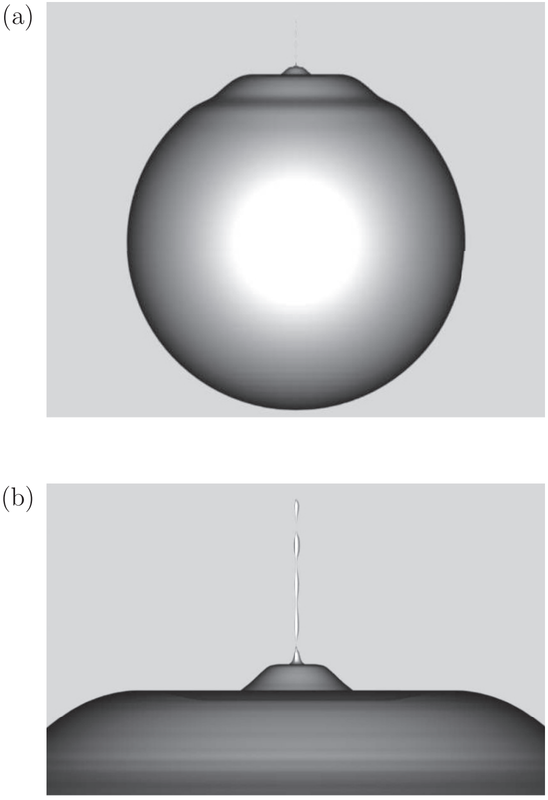

FIG. 18. (a) Three-dimensional jetting event and jet rupture into four tiny droplets. (b) Same event focused on the tiny droplets. $R_m = 0.10$.

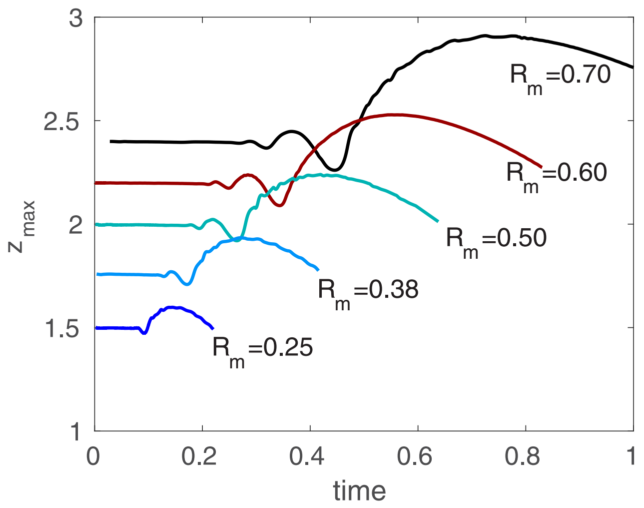

FIG. 19. Maximum axial coordinate $z_{\max}$ evolution for various mother droplet radius until pinch-off.

liquid bridge, $r_{\min}$ and z_{bridge}, respectively. As discussed above, Duchemin *et al.* [8] established that, for inviscid fluids,

$$r_{\min} = D_0 \left(\frac{\gamma R}{\rho}\right)^{1/4} t^{1/2},$$

where D_0 is called the prefactor. Paulsen [10] found that, for low viscosity fluids, his data from $t \in [0.02,0.25]$ and $r_{\min} \in [0.17,0.6]$ follows the power law with a prefactor $D_0 = 1.4$. Simulations performed by Duchemin *et al.* [8] give $D_0 = 1.62$. High speed imaging experiments and other numerical simulations have also checked this scaling regime and all report $D_0 \approx 1$. The Matlab linear fit depicted in Fig. 5 gives the straight line $\log(r_{\min}) = 0.4 \log(t) + 0.13$, from which $D_0 = e^{0.13} = 1.1388$, agreeing amazingly well with the experimental result $D_0 = 1.14$ given in [9].

An idealization of drops coalescing used by many authors, see [6,10], corresponds to a neck of radius $r_{\min}(t)$ and height $z_{\text{bridge}}(t) = r_{\min}(t)^2/R$ connecting two spheres of radius R. To check with the present calculations, Fig. 12 plots $z_{\text{bridge}}(t)$ versus $r_{\min}(t)$ in log-log scale. The computed data follows the mentioned geometrical relation for $r_{\min}(t) > 0.1$, while initially $z_{\text{bridge}}(t) \sim r_{\min}(t)^{2/3}$.

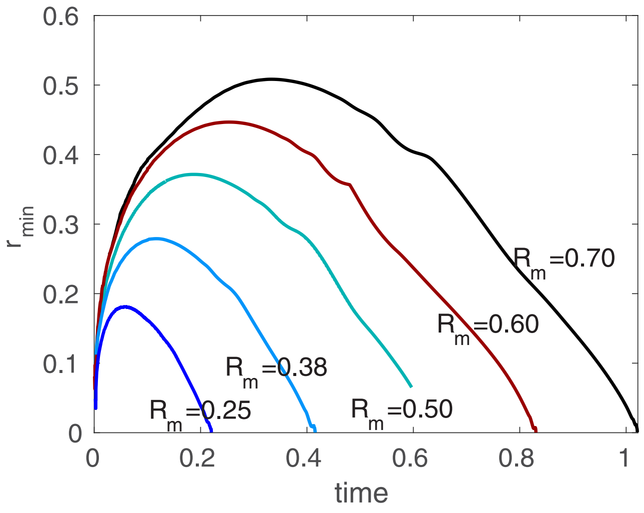

FIG. 20. Minimum neck radius evolution for various mother droplet radius until pinch-off.

As discussed above, the two coalescence regimes proposed recently by Paulsen *et al.* [11], that equally apply for inviscid fluids, are seen in the numerical results, Fig. 5. Clearly there is a sharp change in the slope for dimensionless time $t \sim 0.005$, and as the model is inviscid, either the first regime is due to a mechanism different from viscosity or to numerical viscosity. For droplets with $R = 0.6$ mm this corresponds to $t_c = 8.75\ \mu$s. For 2 mm salt-water droplets the crossover time t_c between these regimes reported in [11] is $t_c = 2\ \mu$s and the corresponding $r_c = 20\ \mu$m. This is in disagreement with the corresponding theoretical values of $t_c = 0.7$ ns and $r_c = 30$ nm proposed in [6,8]. The computed crossover time in this work is also in disagreement with both set of values. We believe these discrepancies are a consequence of the difficulty in obtaining reliable experimental or numerical data at such early stages of bridge formation.

B. Unequal size droplets coalescence

The free surface evolution after the onset of coalescence of two different sized droplets is much richer than the previous case: most noticeably, a satellite drop pinches off depending upon the parent size ratio and the Ohnesorge number [13,16,18]. Following the nomenclature in [18] the bigger and smaller droplets are the father and mother droplets, respectively, and the satellite is the daughter droplet. For the computations presented here we fix the father droplet radius $R_f = 1$ and vary the mother radius R_m in the range $0.1 \leqslant R_m \leqslant 0.9$, allowing a study of the various modes of total or partial coalescence (this terminology will be defined below). Four main patterns have been observed.

(1) Total coalescence. The two droplets simply merge into one mass that evolves until equilibrium is reached. See Fig. 9.

TABLE I. Mother radius, R_m, the parent ratio, $r_{fm} = R_f/R_m$, the daughter radius, R_d, the daughter to mother ratio, $r_{dm} = R_d/R_m$, the nondimensional pinch-off time, t_p, and the normalized pinch-off time $t_p/R_m^{3/2}$. The last column is the coalescence pattern: 1 refers to total coalescence; 2 refers to partial coalescence, first stage; 3 refers to partial coalescence, second stage; 4 is total engulfment with jet emission.

R_m	R_f/R_m	R_d	R_d/R_m	t_p	$t_p/R_m^{3/2}$	Pattern
0.9	1.11					1
0.7	1.43	0.3622	0.52	1.0211	1.74	2
0.6	1.66	0.3133	0.52	0.8304	1.79	2
0.5	2.0	0.2688	0.54	0.6379	1.80	2
0.38	2.63	0.2121	0.56	0.4155	1.77	2
0.25	4.0	0.1431	0.57	0.2203	1.76	2
0.20	5.0	0.1094	0.55	0.1553	1.74	3
0.15	6.67	0.0820	0.55	0.1052	1.81	3
0.10	10					4

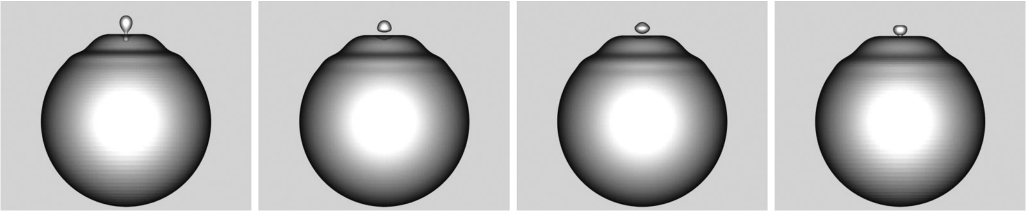

FIG. 21. Three-dimensional snapshots at $t = 0.1052, 0.118, 0.1224, 0.1285$ of pinch-off profile and daughter droplet oscillations, $R_m = 0.15$.

(2) Partial coalescence, first stage. The droplets merge and soon after a first daughter droplet pinches off. After subsequent reconnection, smaller droplets may pinch off. See Figs. 13–15.

(3) Partial coalescence, second stage. Here the first daughter droplet pinch off is not seen (at least it is missed in laboratory experiments), but subsequent smaller droplet pinch-off may occur. See Fig. 16.

(4) Total engulfment followed by jet ejection. In this mode, the capillary wave created upon first contact is too weak to create a daughter droplet. The mother droplet is absorbed by the father droplet and inertia creates a cavity from which a tiny jet is ejected. See Figs. 17 and 18.

The terms partial coalescence, first and second stage, were taken from [18]. In their laboratory experiments for Ohnesorge numbers greater than zero, partial coalescence first stage refers to a visible pinch-off of a daughter droplet whose size is approximately half of the mother droplet. Second stage pinch-off refers to the lack of completion of first pinch-off (at least it was not observable) followed by, at a later time, a much smaller daughter droplet pinch-off. We have adopted these terms as they match some of the patterns observed in our numerical experiments.

The fixed computational domain is $\Omega_D = [-1.5, 1.5] \times [-2, 3.5]$ with grid size $\Delta r = 0.005$, giving sufficient resolution for the level set computations. The free boundary is initially two circles of radii R_f and R_m touching at $z = 1$, and as before, the initial velocity potential on the front is set to zero, $\phi(r,z,0) = 0$. The onset of coalescence is modeled in the same manner as for two equal size droplets. Briefly, at any discrete time t_n, the free boundary is extracted from the zero level set of $\Psi(t_n)$ using a first order approximation. A new set of nodes is redistributed along this polygonal line [20], allowing an increased spatial resolution near singular events (merging or breaking of the fluid domain). The typical spacing between points on the front ranges from $\Delta s \approx 0.02$ near coalescing or pinch-off, to $\Delta s = 0.035$; the evolution is smooth. Clearly, tiny daughter droplets also need a more resolved grid and we set $\Delta s = 0.005$ in this situation.

The term partial coalescence indicates the appearance of a secondary (daughter) drop visible above the bulk of the fluid. Of interest in this context is to identify the parameter regimes that result in partial or complete coalescence and what determines the ratio of the daughter radius to the mother radius. The general flow pattern after the onset of coalescence, seen in laboratory experiments [18] and simulations [16], can be summarized as follows: a visible capillary wave generated by droplet merging propagates through the free surface, converging rapidly at the top of the mother droplet and creating a near cylindrical protrusion. This pattern is seen for inviscid and viscous fluids, but in the latter case the capillary wave is damped due to viscous forces. Whether this cylindrical protrusion will collapse vertically or will pinch off horizontally remains a matter of discussion. Within the present study we are not able to establish the dependence on the Ohnesorge number, but we can analyze in detail the different flow patterns and daughter radius for a wide range of relative drop sizes, $0.1 \leqslant R_m \leqslant 0.9$.

To give an idea of how the cylindrical protrusion $z_{\max}$ and the minimum neck radius $r_{\min}$ evolve, we plot these variables, for various values of R_m and versus time, in Figs. 19 and 20, respectively. We can observe the times at which the capillary wave reaches the top of the unified fluid mass, and this approximately corresponds to the time at which $r_{\min}$ starts decreasing. The increase in the wave amplitude seen in Fig. 19 is a signal that fluid is being removed rapidly towards the top of the drop, causing the onset of the pinching neck at the bottom of the protruding cylinder.

As can be seen from Table I for $0.15 \leqslant R_m \leqslant 0.7$ a daughter droplet pinches off with a ratio $r_{dm} = R_d/R_m$ between 0.52 and 0.57. This is in very good agreement with previous experiments and numerical simulations. Moreover, we can further distinguish different pinch-off patterns within this range of R_m values: for $0.15 \leqslant R_m < 0.25$ pinch-off occurs at the reentrant surface of the father droplet below its maximum axial coordinate. It would be unlikely that this event would be seen in laboratory experiments. Between $0.25 \leqslant R_m \leqslant 0.50$, the daughter droplet pinches off completely above the top of the parent droplet with a small tail that recoils rapidly towards the daughter droplet. When $0.6 \leqslant R_m \leqslant 0.7$, the daughter tail is considerably longer, giving rise to the formation of a

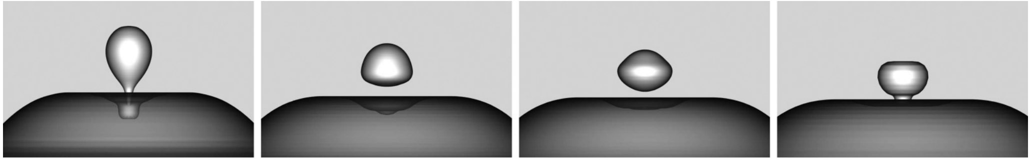

FIG. 22. Three-dimensional focused snapshots at $t = 0.1052, 0.118, 0.1224, 0.1285$ of pinch-off profile and daughter droplet oscillations, $R_m = 0.15$.

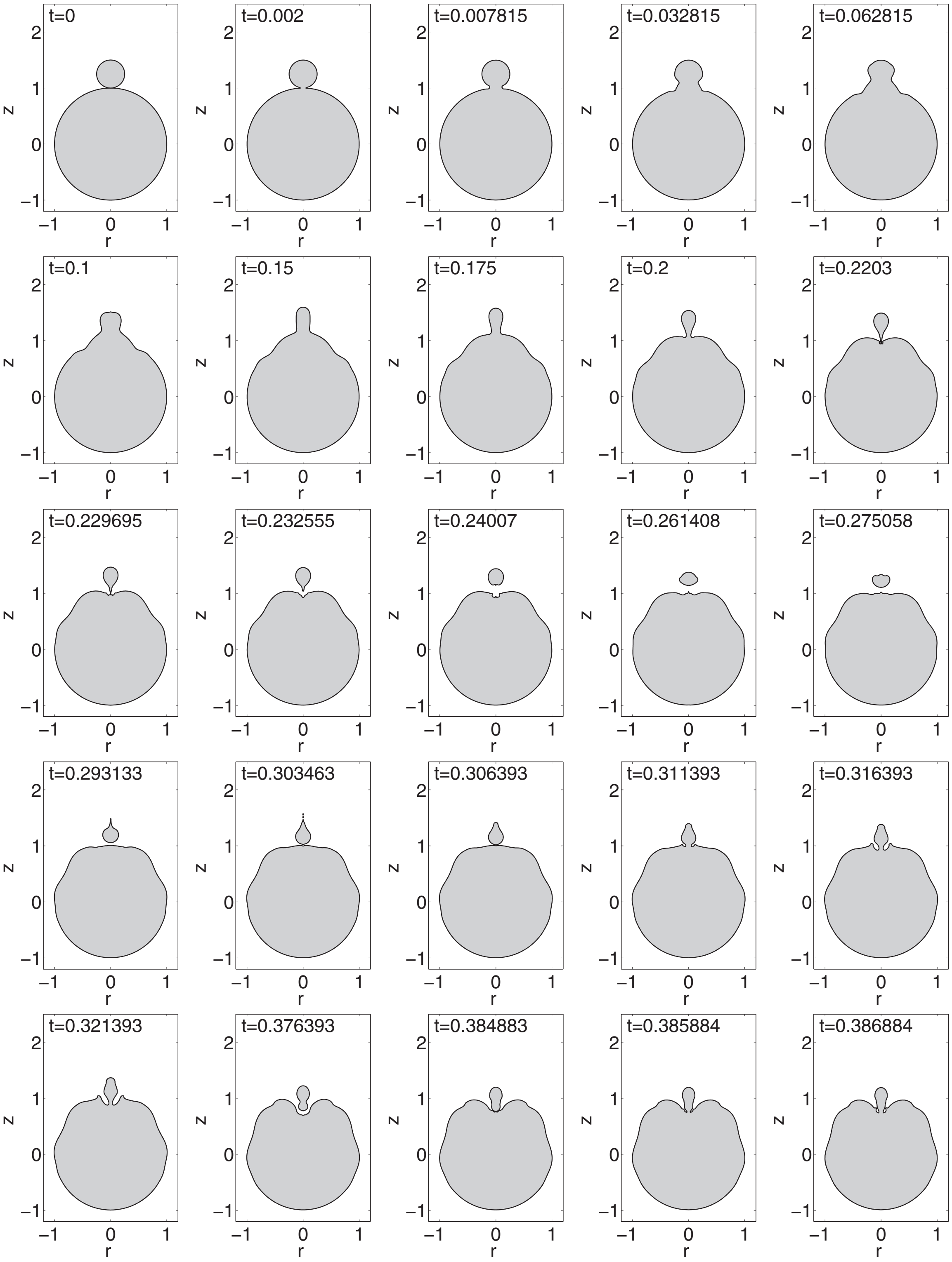

FIG. 23. Complete sequence of two drops, $R_1 = 1, R_2 = 0.25$ coalescing at indicated times.

tiny tertiary droplet. To illustrate these distinct patterns of partial coalescence, Figs. 13–16 display a short sequence of front shapes through pinch-off, for $R_m = 0.7$, 0.6, 0.38, and 0.15, respectively. For the figure with $R_m = 0.15$, we have chosen to keep the scaling of the r,z axis equal to the previous figures to have a notion of the different droplet dimensions. Figures 21 and 22 display 3D renderings of the two droplets as well as focused front shapes after pinch-off, both for $R_m = 0.15$. In this case the daughter droplet detaches and evolves independently for approximately 7 ns, whereupon it merges again with the main droplet. The post-pinch-off events mostly occur inside the upper hole of the big droplet and thus could not be seen in a laboratory experiment. We therefore classify this pattern as second stage coalescence, provided a second

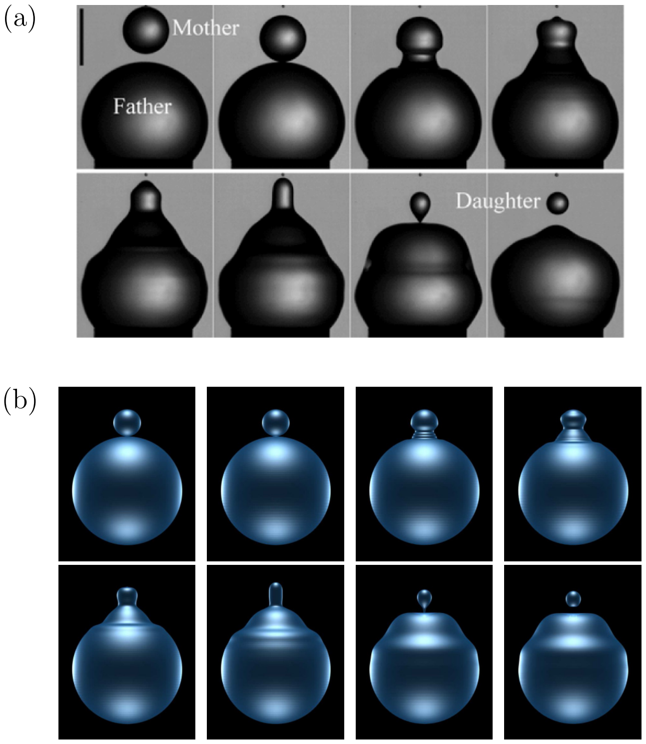

FIG. 24. (a) Laboratory experiments for distilled water droplets, $R_f/R_m = 2.72$, taken from [18]; coalescence starts on the second panel where subsequent images are shown at 0.27,0.67,0.93,1.2,1.8, and 4.6 ms later. The scale bar is 1 mm. (b) Computational result corresponds to $R_f/R_m = 4$.

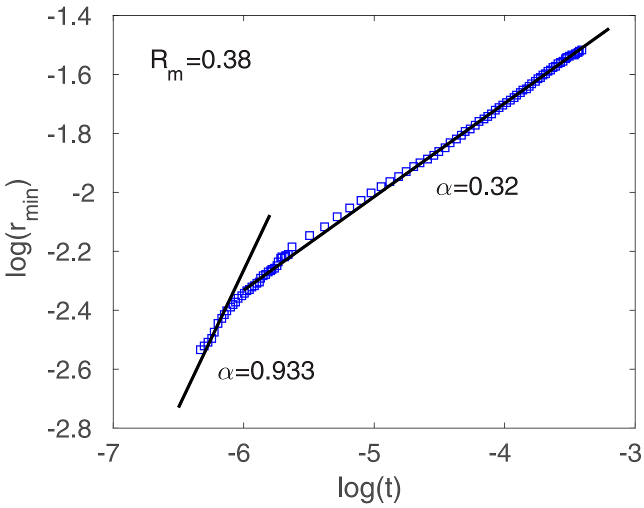

FIG. 26. Minimum neck radius evolution when the bridge is expanding and scaling exponents for $R_m = 0.38$. Base-e logaritms.

ejection of a smaller droplet will occur. It is possible to find a 3D movie of the coalescence process for $R_m = 0.15$ in the Supplemental Material [29].

The last coalescence mode is found for $R_m \leqslant 0.1$ wherein total engulfment of the mother droplet occurs. The suction evolves creating a hole in the top of the main mass and the subsequent expansion is accompanied by a jet ejection and disintegration into very tiny droplets. This sequence of events and focused ejection profiles are shown in Figs. 17 and 18, respectively.

Another important flow feature is the time elapsed between the onset of coalescence and pinch-off. The nondimensional equations are based on a characteristic length scale $r_0 = 1$ and time scale $t_0 = \sqrt{\frac{\rho}{\gamma} r_0^3}$. If we want to compare our times to pinch-off times normalized by $t_m = \sqrt{\frac{\rho}{\gamma} R_m^3}$, as in [18], we have to divide our computed pinch-off time by $R_m^{3/2}$, displayed in the sixth column of Table I. This normalized value is almost constant with an average value of 1.78, in very good agreement with values reported in [16,18].

Previous and very complete numerical simulations [16] report the difficulties in describing the small scale motions after pinch-off of the daughter droplet and before a second coalescence takes place. In contrast, we are able to easily compute pinch-off and past pinch-off events until a second coalescence occurs. In Fig. 23, a complete sequence of the front

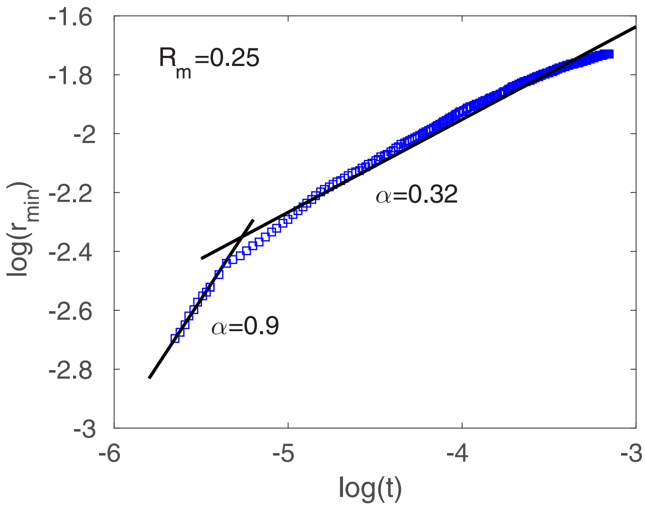

FIG. 25. Minimum neck radius evolution when the bridge is expanding and scaling exponents for $R_m = 0.25$. Base-e logarithms.

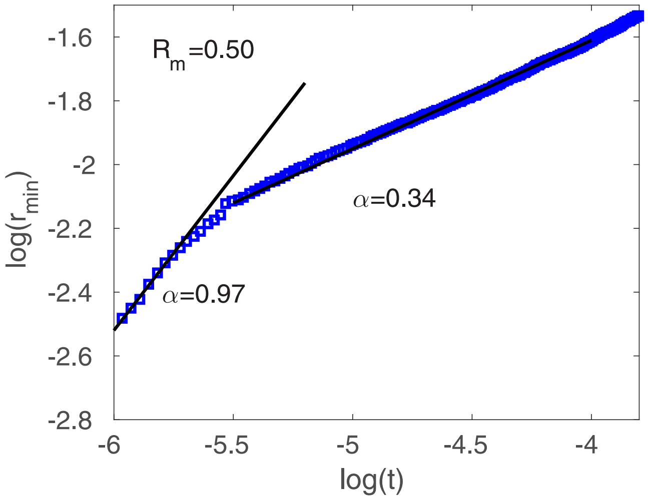

FIG. 27. Minimum neck radius evolution when the bridge is expanding and scaling exponents for $R_m = 0.50$. Base-e logarithms.

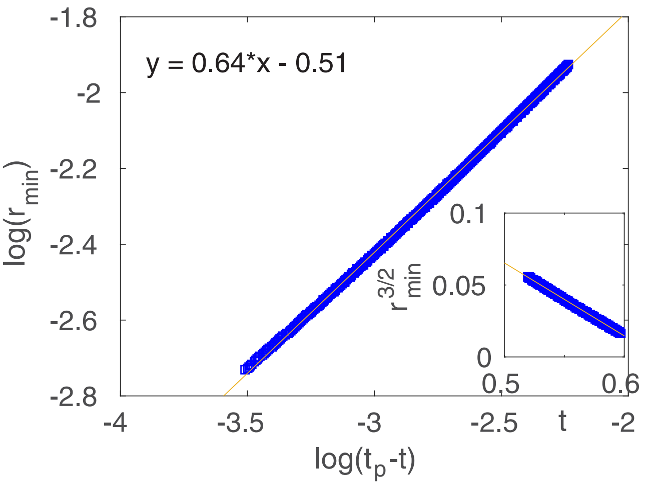

FIG. 28. Minimum neck radius evolution before daughter droplet pinch-off and scaling exponents for $R_2 = 0.50$. Base-e logarithms.

evolution is depicted for $R_m = 0.25$. At dimensionless time $t = 0.386884$ the computation is stopped because air mass is visibly trapped near the neck and the code is not prepared to handle such a situation. However, we believe that this mass of trapped air could contribute to the detachment of a second droplet, reported in experiments to have a radius of 18% of the mother droplet.

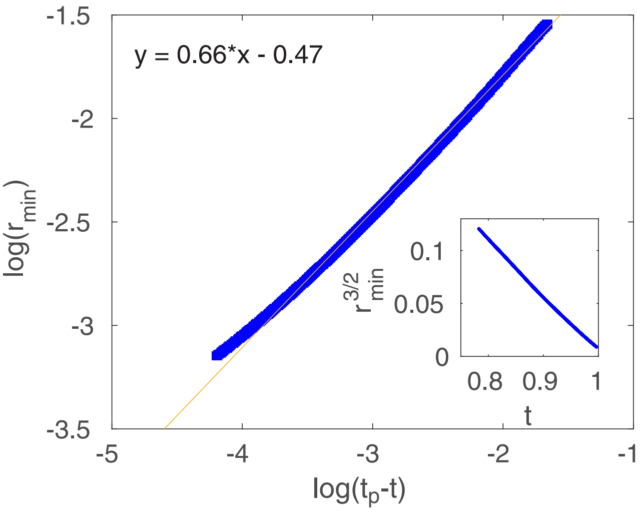

FIG. 29. Minimum neck radius evolution before daughter droplet pinch-off and scaling exponents for $R_2 = 0.70$. Base-e logarithms.

TABLE II. Mother radius, R_m, the scaling exponent at the onset of coalescence, α_1, the persisting scaling exponent for the bridge expansion, α_2, and the daughter droplet pinch-off scaling exponent, α_3.

R_m	α_1	α_2	α_3
0.7	0.25	0.38	0.66
0.6	0.78	0.38	0.68
0.5	0.97	0.34	0.64
0.38	0.93	0.32	0.64
0.25	0.9	0.32	0.63

Some additional comments are in order. Although we have been motivated by the experiments of unequal droplet coalescence presented in [18], the only comparison we can legitimately carry out is with their distilled water experiment for drops with $R_f/R_m = 2.72$ (their Fig. 1). The remainder of their experimental results involve drops of 30% glycerin with an Ohnesorge number of 0.0116. The simulated results for inviscid liquids do not show as great a variability as their experiments: instead partial coalescence (first stage) is very persistent in the range $1.43 \leqslant R_f/R_m \leqslant 4$. We found a critical parent ratio of $R_f/R_m = 1.43$ above which a satellite is produced. The critical parent ratio reported in [18] is 1.55 for Ohnesorge number equal zero agrees well with our computed critical parent ratio of 1.43.

For visual comparison, Fig. 24 displays the computed profiles (b) and the water droplets laboratory experiments (a). The laboratory photographs taken from [18] correspond to distilled water drops with $R_f/R_m = 2.72$, whereas the three-dimensional renderings correspond to similar events for $R_m = 0.25$. To observe dynamically this sequence of events we refer to the Supplemental Material [29].

Scaling laws and self-similarity

Here we investigate whether the coalescence process of two unequal drops can be considered self-similar, i.e., independent of initial conditions. In the present study the initial conditions vary solely with the size of the mother droplet, R_m. With this as the characteristic length scale, the size of the rescaled daughter droplet is always between 0.52 and 0.57 and the rescaled pinch-off time is between 1.74 and 1.81, in very good agreement with the reported values in [16,18]. This is a good initial indicator of self-similarity, but further studies can be performed using the simulations.

As in the case of two equal size droplets, the scaling law of the minimum neck radius during the expansion of the connecting bridge can be investigated. By plotting $\log(r_{\min})$

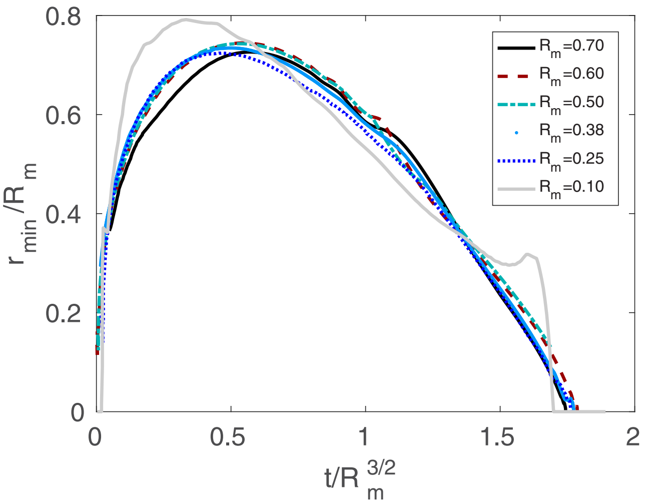

FIG. 30. Normalized minimum neck radius, $r_{\min}/R_m$, versus normalized time, $t/R_m^{3/2}$, for $R_m = 0.10, 0.25, 0.38, 0.50, 0.60, 0.70$. The collapse of all curves indicates the self-similar behavior of the minimum neck radius.

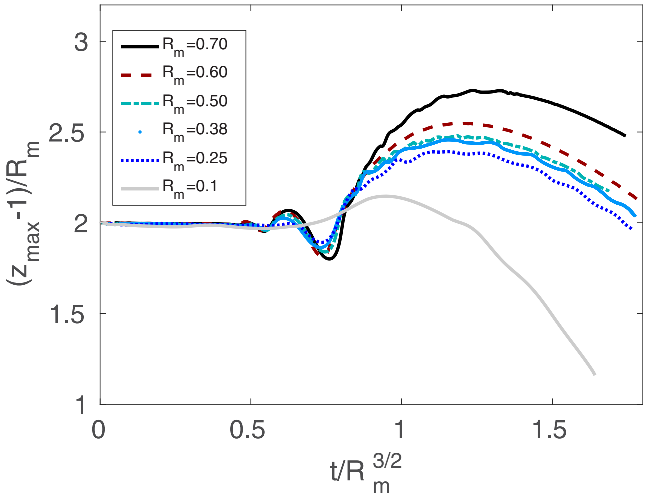

FIG. 31. Normalized elevation with respect to $z=1$ $(z_{\max}-1)/R_m$, versus normalized time, $t/R_m^{3/2}$, for $R_m = 0.10, 0.25, 0.38, 0.50, 0.60, 0.70$. The collapse of the curves for $0.25 < R_m < 0.60$ indicates the self-similar behavior of this variable in the partial coalescence pattern without tertiary droplet. The curve for $R_m = 0.70$ departs above pointing out the tertiary droplet formation and $R_m = 0.10$ departs below indicating total engulfment.

versus $\log(t)$ for $R_m \in [0.25, 0.70]$ we again found two distinct self-similar exponents: α_1 at the very initial onset of coalescence and α_2 the more persisting bridge expansion exponent. The log-log plots with the corresponding exponents (Matlab fits) for $R_m = 0.25, 0.38, 0.50$, are given in Figs. 25–27, respectively.

Second, the well known scaling for inviscid pinch-off, $r_{\min} \approx \tau^{2/3}$, with $\tau = t_p - t$ the time to pinch off, is investigated. We plot in logarithmic scale $r_{\min}$ versus $(t_p - t)$ for $R_m \in [0.25, 0.70]$. Figures 28 and 29 show these results for $R_m = 0.50, 0.70$, the linear fit again from Matlab. The inset in these figures shows also $r_{\min}^{3/2}$ versus time, necessarily a straight line from which the value of t_p is obtained. The pinch-off scaling exponent α_3 lies in the interval $[0.64, 0.68]$ for all cases, in very good agreement with both theory and experiments. Table II summarizes all of the computed self-similar scaling exponents.

Armed with this information, Fig. 30 plots the normalized minimum neck radius $r_{\min}/R_m$ versus the normalized time $t/R_m^{3/2}$ for $t \in [0, t_p]$. All of the curves in Fig. 20 collapse onto one curve, highlighting the self-similar behavior for this flow variable in the case of partial coalescence. Included in this figure is the curve corresponding to $R_m = 0.1$, showing that it does not match the other curve, thereby indicating a distinct coalescence pattern, i.e., total engulfment.

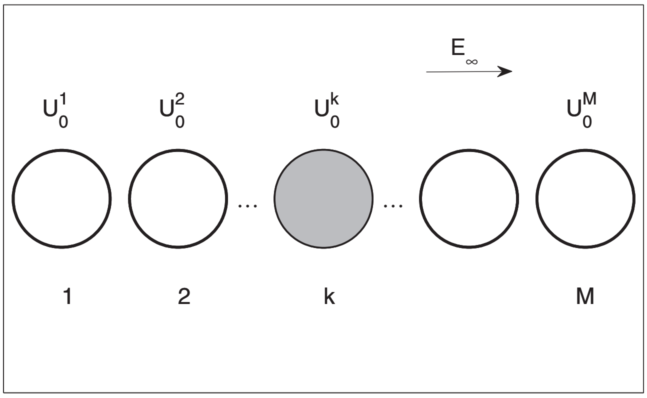

FIG. 32. M inviscid droplets interacting under electric forces.

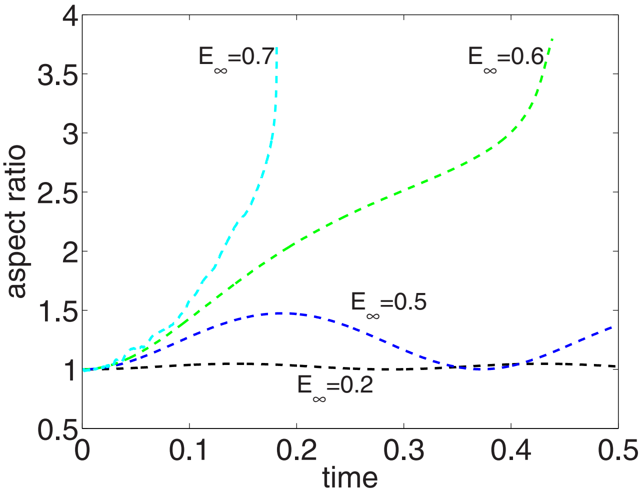

FIG. 33. Aspect ratio evolution for one drop of radius $r_o = 0.25$ for various field intensities.

The other relevant geometric variable is the upward stretching of the cylindrical column before the onset of pinching, $z_{\max}$, Fig. 19. To gain some insight about the behavior of this variable Fig. 31 plots $(z_{\max} - 1)/R_m$ versus the normalized time $t/R_m^{3/2}$ for $t \in [0, t_p]$. Note that $(z_{\max} - 1)$ indicates the elevation with respect to the common contact point at $z = 1$. This graph turn out to be quite revealing and serves to classify the coalescence pasterns found in the simulations. For $0.25 < R_m < 0.60$ all curves collapse into one—the partial coalescence without tertiary droplet mode. The $R_m = 0.70$ curve departs significantly upwards for normalized time $t/R_m^{3/2} > 1$,

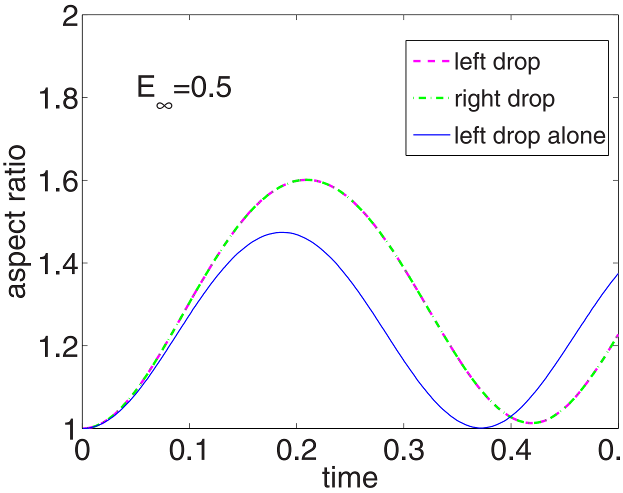

FIG. 34. Aspect ratio evolution for two drops of radius $r_o = 0.25$. The amplitude and oscillating period of the interacting drops are equal but distinct of these quantities if only the left drop were present.

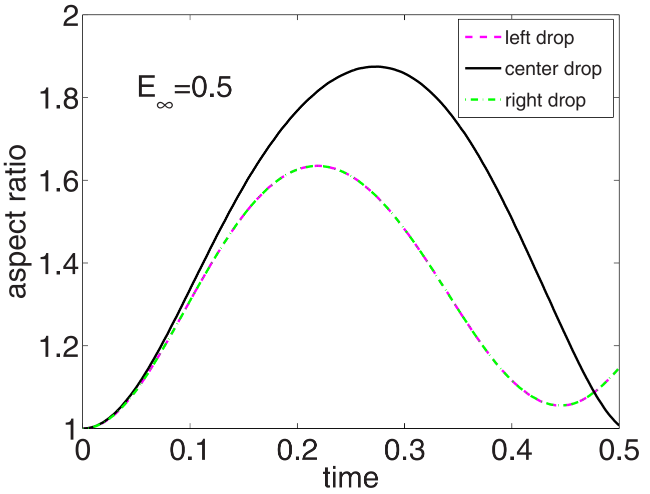

FIG. 35. Aspect ratio evolution for three drops of radius r_o=0.25. The amplitude and oscillating period of the central drop is distinct from left and right droplet oscillating parameters.

indicating the longer daughter droplet tail and subsequent tertiary droplet formation. For $R_m < 0.15$ the behavior of $(z_{\max} - 1)$ is completely different, and this corresponds to total engulfment.

V. ELECTROHYDRODYNAMIC DROPLET COALESCENCE

Pioneer work on the distortion and disintegration of water droplets subject to electric fields is due to Taylor; see [30,31]. More recent works, among many others, can be found in [32–35]. Nowadays the use of electric fields to enhance water droplet coalescence is very common in, for example, the treatment of emulsions [36], the fabrication of Janus and patchy capsules [37], and the design of microfluidic devices [38].

A. Electrical droplet interaction

Numerical studies of the distortion and destabilization of a charged or uncharged water droplet subject to a uniform electric field have been presented in [23]. These simulations added an electric field solver to the inviscid breakup algorithm that forms the basis for the present studies, so it is relatively straightforward to investigate the coalescence of several droplets in the presence of an exterior uniform field of intensity E_∞. The theoretical formulation was detailed in [23], but for completeness it is reviewed here.

We want to study the electrodynamics of M inviscid liquid droplets under the action inertia, capillary, and electrical forces. The governing equations for the hydrodynamics are Eqs. (1)–(10), with now

$$\Omega_1(t) = \cup_{k=1}^{M} \Omega_1^k, \quad \Gamma(t) = \cup_{k=1}^{M} \Gamma_k(t),$$

and Ω_D a fixed domain that contains the free boundary $\Gamma(t)$ for all times. These equations have to be coupled with the electrodynamics in the exterior infinite domain $\Omega_2(t)$,

$$\mathbf{E} = -\nabla U \quad \text{in } \Omega_2(t), \tag{32}$$

$$\Delta U = 0 \quad \text{in } \Omega_2(t), \tag{33}$$

$$U = U_0^k(t) \quad \text{on } \Gamma_k(t), \quad k = 1, \ldots, M, \tag{34}$$

$$U = -E_\infty z \quad \text{at infinity}, \tag{35}$$

where the electric potential on each drop free boundary, $U_0^k(t)$, has to be obtained. A sketch of the physical situation in given in Fig. 32.

The axisymmetric Laplace equation governs the velocity potential ϕ interior to, and the electric potential U exterior to, the fluid. The boundary integral formulation, based upon a linear element Galerkin approximation, has been presented elsewhere [27], so the discussion here is limited to the method for obtaining the electric field boundary conditions (34).

To include the uniform field at infinity, we define the modified potential function $\tilde{U}$ as

$$U = \tilde{U} - E_\infty z. \tag{36}$$

As a consequence, $\Delta\tilde{U} = 0$, the boundary condition on the fluid surface is $\tilde{U} = U_0 + E_\infty z$, and $\tilde{U}$ vanishes at infinity (and is therefore suitable for an exterior boundary integral solution). For a single fluid drop, an equation for the unknown U_0 is easily obtained from the condition of zero charge (or a given charge q) inside the droplet, namely

$$0 = \int_\Sigma \frac{\partial U}{\partial n} d\Sigma = \int_\Sigma \frac{\partial \tilde{U}}{\partial n} d\Sigma - E_\infty \int_\Sigma n_z d\Sigma, \tag{37}$$

where Σ is the full three-dimensional surface. Using the axisymmetry, these integrals are converted to integrals over $\Gamma(t)$ in the usual manner. As the free front boundary condition for the vanishing potential $\tilde{U}$ is $\tilde{U} = U_0 + E_\infty z$, the flux $\partial\tilde{U}/\partial n$ is composed of two parts: let u_n^z be the flux resulting from the boundary condition $E_\infty z$ and u_n^1 the flux when the boundary condition is the potential $U_0 = 1$ (in both cases the zero boundary condition at infinity holds). Then

$$\frac{\partial \tilde{U}}{\partial n} = U_0 u_n^1 + u_n^z \tag{38}$$

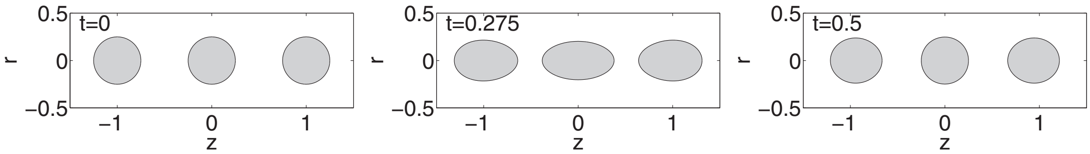

FIG. 36. Electrical interaction of three droplets under $E_\infty = 0.5$. Drop profiles at $t = 0$, $t = 0.275$, time at which the central droplet is at its maximum distortion, and $t = 0.5$.

and Eq. (37) becomes

$$U_0 \int_\Sigma u_n^1 d\Sigma = E_\infty \int_\Sigma n_z d\Sigma - \int_\Sigma u_n^z d\Sigma. \qquad (39)$$

This determines U_0.

For M interacting drops, there is a different constant potential U_0^k on each, but there is also a separate charge equation for each drop. However, as the drops interact, the potentials cannot be determined independently: a system of linear equations for $\{U_0^k\}$ must be constructed and solved. For $k = 1,\dots,M$, we can write

$$0 = \int_{\Sigma_k} \frac{\partial U}{\partial n} d\Sigma = \sum_{j=1}^{M} \left\{ U_0^j \int_{\Sigma_k} U_n^{jk} d\Sigma \right\} - E_\infty \int_{\Sigma_k} n_z d\Sigma + \int_\Sigma u_n^z d\Sigma, \qquad (40)$$

where U_n^{jk} is the flux on Σ_k that results from setting the potentials to $U_0^\ell = \delta_{j\ell}$, i.e., equal to 1 on Σ_j and zero on all other drops. This provides the order M linear system needed to obtain $\{U_0^k\}$. This procedure can also be employed if the conducting drops are not charge neutral. In this case, each drop charge q_k, $k = 1,\dots,M$, in Eq. (40) must be specified.

Several numerical experiments have been conducted to test the droplet electrical interaction algorithm. First, a single droplet of radius $R = 0.25$ is set in motion by applying electrical fields of different intensity $E_\infty = 0.2, 0.5, 0.6, 0.7$. A critical value above which the droplet will destabilize is found to be $E_\infty^c = 0.6$; see Fig. 33. This is in fact in accordance with the theoretical $E_\infty^c = 0.3$ for $R = r_0 = 1$ and electrical field intensity scale $E_0 = (\sqrt{2\gamma/\epsilon})r_0^{-1/2}$; see [23,39]. To further clarify, as $E_0 \approx r_0^{-1/2}$ if we want to normalize the critical field intensity for $R = r_0 = 0.25$ we have to divide the computed critical field intensity, $E_\infty^c = 0.6$, by $r_0 = (0.25)^{-1/2} = 2$, which agrees with the previous 0.3 value.

Next, two neutral droplets of radius $R = 0.25$, separated a distance of $d = 0.50$, are subjected to an electric field of intensity $E_\infty = 0.5$. By symmetry, these two droplets should oscillate with the same frequency, but this frequency should be different from the single drop calculation; see Fig. 34. Instead, two droplets of radius $R = 1$, separated also a distance of $d = 0.50$ and subject to $E_\infty = 0.5$, will merge into a bigger droplet. This bigger water mass will elongate in the direction of the electric field and jet ejection will occur from Taylor cones at both droplet ends. It is possible to visualize the complete process (see the Supplemental Material [29]). A vast number of simulations will be needed to obtain the parameter diagram for the various coalescence modes in terms of the normalized drop separation d/R and electric field intensity E_∞. This investigation will be developed in future work. For completeness the case of three equal drops, radius $R = 0.25$, interacting under the same electric field is considered. Figure 35 displays the aspect ratios versus time, while Fig. 36 shows the droplets shapes at $t = 0$, $t = 0.275$, and $t = 0.5$. In this case, the central droplet is pulled by the electric field as well as by the side droplets, and thus it oscillates with a higher amplitude and period than the identical left and right droplets. Unfortunately, for multiple droplet interaction, there is a dearth of experimental or analytical results that could be used to further validate the code.

TABLE III. Electric field intensity, E_∞, the daughter radius, R_d, the daughter to mother ratio, $r_{fm} = R_d/R_m$, and the nondimensional pinch-off time, t_p.

E_∞	R_d	R_d/R_m	t_p
0	0.2121	0.558	0.4154
0.05	0.2136	0.5621	0.4140
0.1	0.2195	0.578	0.4212
0.15	0.2261	0.595	0.4256
0.2	0.2371	0.624	0.4345
0.22	0.2429	0.639	0.4397

The next section applies this code to study how the presence of an electric field alters the coalescence flow characteristics.

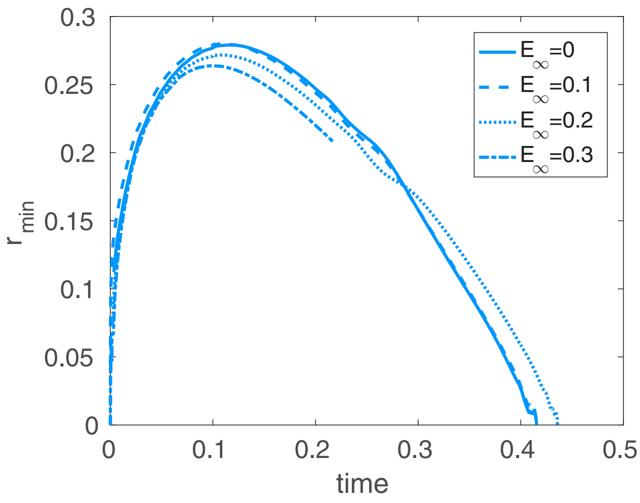

FIG. 37. Minimum neck radius evolution for various electric field intensities until pinch-off, except for $E_\infty = 0.3$ for which the drop will not pinch-off but burst.

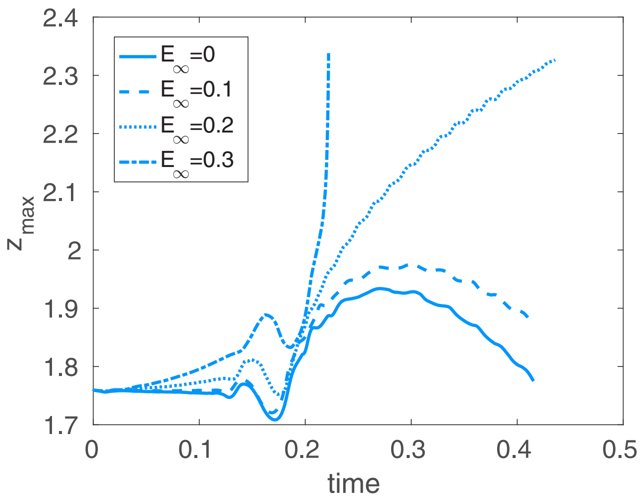

FIG. 38. Maximum axial coordinate evolution for various electric field intensities until pinch-off, except for $E_\infty = 0.3$ for which the drop will not pinch-off but burst.

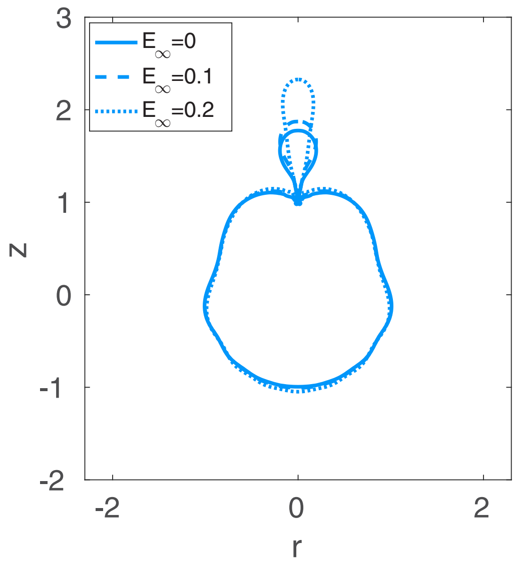

FIG. 39. Superimposed droplet profiles at pinch-off for R_m=0.38 and various electric field intensities $E_\infty = 0.,0.1,0.2$.

B. Electrical droplet coalescence

Of particular interest is how the uniform electric field might change the size of the daughter droplet in the coalescence process. We focus on the range of mother droplet radius for which partial coalescence is self-similar, $0.25 < R_m < 0.6$; it will suffice to run numerical simulations for a fixed value, $R_m = 0.38$. The only parameter left in the nondimensional model is the nondimensional far field electric field intensity and the solution for $E_\infty = 0.1, 0.2, 0.3$ will be compared to that for $E_\infty = 0$. In Figs. 37 and 38 the evolution of the minimum neck radius $r_{\min}$ and the maximum axial coordinate $z_{\max}$ are shown. The evolution of $r_{\min}$ is quite similar to the zero field $E_\infty = 0$ case, but $z_{\max}$ is much more interesting. For values $E_\infty \geqslant 0.3$ the coalesced drop will destabilize and a fine jet will be emitted from its top. Between $0 \leqslant E_\infty \leqslant 0.2$ a daughter droplet will pinch off with a radius that increases with the electric field intensity. Table III presents a summary of the flow characteristics for various values of the electric field intensity.

It has been observed that, with an applied electric field, the droplet profiles at the onset of coalescence and the evolution of the connecting bridge are very similar to those of free coalescence ($E_\infty = 0$). However, the postcoalescence vertical stretching of the protruding cylinder increases significantly with the intensity of the electric field. In particular, for $E_\infty = 0.2$, daughter pinch-off occurs when $z_{\max}$ is still growing, as it can be seen in Fig. 38, causing the droplet to oscillate at a much higher z level. To see how the pinching profiles change with E_∞, Fig. 39 superimposes the droplet profiles for several values of E_∞.

After pinching, the daughter droplet and main droplet are oppositely charged. They continue to reconnect and disconnect for a short period of time, and also stretch out due to the electric field. We have not continued these simulations; instead the electric field is switched off, $E_\infty = 0$, just after pinch-off. The size of the daughter droplet is then maintained, and it quickly recoils and oscillates at a higher frequency and elevation: see the sequence of events depicted in Fig. 40. In Fig. 41 it is shown that, for $E_\infty = 0.3$, coalescence takes place followed by jet emission at $t = 0.2424$. To obtain a sharper value for the critical electric intensity, E^c_∞, above which the droplet will destabilize, more simulations are performed in the range $0.2 < E_\infty < 0.3$, and we found that $0.22 < E^c_\infty < 0.225$, the reason for which the maximum ratio R_d/R_m attainable is

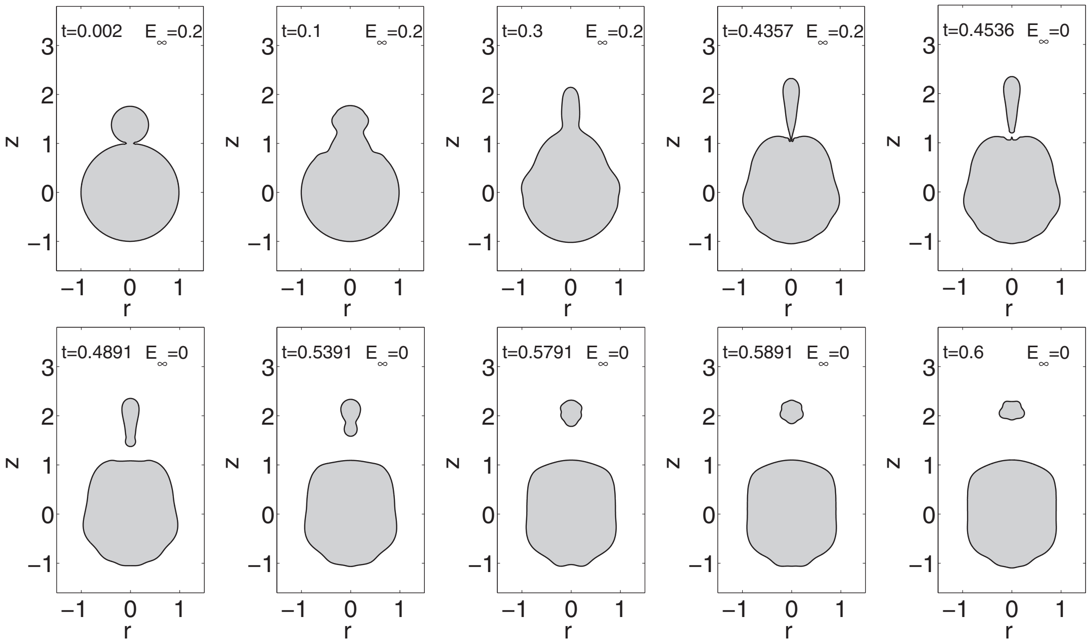

FIG. 40. Snapshots of electrohydrodynamic partial coalescence for $R_m = 0.38$ and $E_\infty = 0.2$. At pinch-off time the electric field is turned off ($E_\infty = 0$).

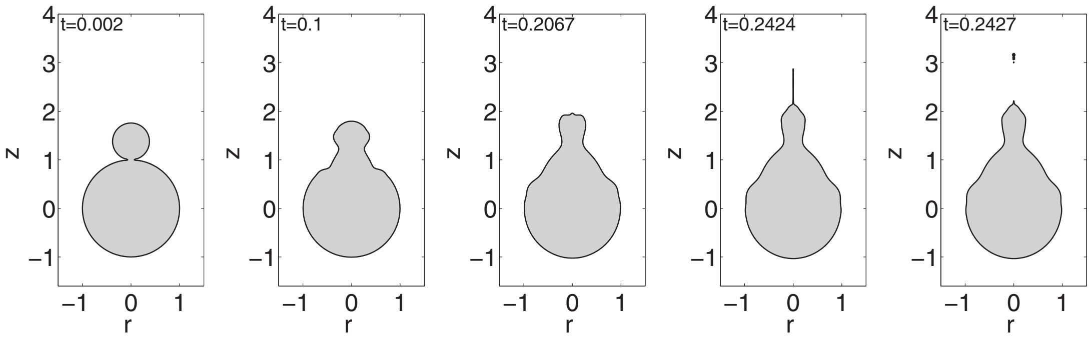

FIG. 41. Snapshots of electrohydrodynamic partial coalescence for $R_m = 0.38$ and $E_\infty = 0.3$. The drop destabilizes and jet emission starts at $t = 0.2367$.

0.639, at least for $R_m = 0.38$. For values $E^c_\infty \geqslant 0.225$ jet ejection will occur preventing the formation of a daughter droplet. Finally, to be able to predict the size of the daughter droplet, Fig. 42 plots r_{dm} versus the applied electric field intensity E_∞. From a Matlab quadratic fit we have obtained the relationship

$$r_{dm} = 1.6E^2_\infty + 0.018E_\infty + 0.56.$$

More simulations are needed to explore the effect of the electric field intensity for different values of R_f/R_m and this will hopefully be taken up in a future work.

Numerical simulations have demonstrated that an applied electric field can control the size of the daughter droplet released during the partial coalescence of unequal father and mother droplets. Specifically, for $R_f/R_m = 2.63$ and E_∞ within the range $0 < E_\infty < 0.225$, it is possible to increase the size of the daughter droplet and have it oscillate at a higher z level and frequency by turning off the electric field at pinch-off time.

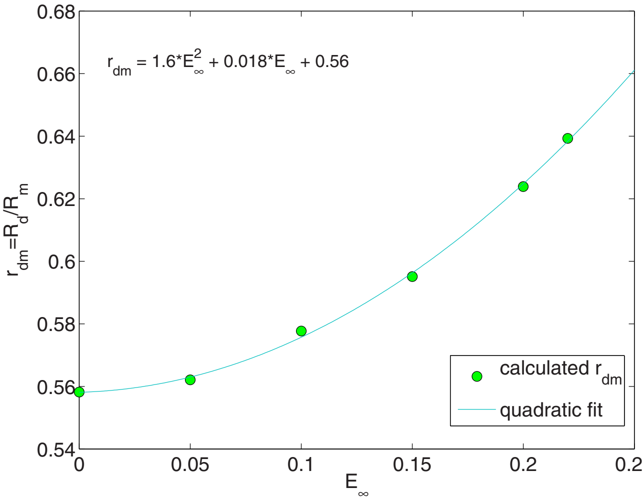

FIG. 42. Calculated ratios $r_{dm} = R_d/R_m$ versus electrical field intensity, E_∞, and quadratic fit.

VI. CONCLUSION

An embedded potential flow model has been used to numerically study the coalescence of two inviscid droplets, without any need to impose an existing initial bridge. The calculations seamlessly follow the free surface through singular events, the breakup and merging of fluid domains. For equal sized initial droplets, the scaling laws for the radial and axial bridge evolution have been studied in detail and compared with existing works. The computed coalescence profiles and time occurrences are in very good agreement with laboratory experiments [13].

For two unequal sized initial droplets, simulations covering a wide range of parent size ratios, $1 \leqslant R_f/R_m \leqslant 10$, have been carried out. We have been able to classify the different coalescence patterns that depend only upon the parent droplet ratio, and we confirm the self-similar behavior of partial coalescence for $1.66 < R_f/R_m < 4$. The computed size of the daughter droplet and the pinch-off time matches previous numerical studies [16] and with laboratory experiments. The computed three-dimensional renderings look very much like the experimental photographs for distilled water droplets presented in [18].

The effect of an electric field on the partial coalescence process has also been investigated. The solution of the electric field problem is easily incorporated within the embedded potential flow model. Numerical simulations were performed to determine the influence of the electric field intensity on the size and shape of the daughter droplet. For values of the electric field intensity below the critical one, it is possible to control the size and elevation of the daughter droplet. A quadratic relationship between the intensity of the applied electric field and the ratio R_d/R_m has been obtained.

ACKNOWLEDGMENTS

This work was supported in part by the Applied Mathematical Science subprogram of the Office of Science, U.S. Department of Energy, under Contract No. DE-AC02-05CH11231. The first author was also supported by the Spanish Ministry of Economy and Competitiveness. State Research Agency, Project No. MTM2017-87162P. All three-dimensional renderings have been made by Fernando Villalon with Blender.

[1] N. Snook and M. Xue, Geophys. Res. Lett. **35**, 24803 (2008).
[2] J. D. Yu, S. Sakai, and J. A. Sethian, Interfaces Free Bound. **5**, 459 (2003).
[3] I. Marginean, P. Nemes, and A. Vertes, Phys. Rev. E **76**, 026320 (2007).
[4] W. D. Ristenpart, J. C. Bird, A. Belmonte, F. Dollar, and H. A. Stone, Nat. Lett. **461**, 377 (2009).
[5] S. Nudurupati, M. Janjua, P. Singh, and N. Aubry, Phys. Rev. E **80**, 010402(R) (2009).
[6] L. Duchemin, J. Eggers, and C. Josserand, J. Fluid Mech. **487**, 167 (2003).
[7] A. Menchaca-Rocha, A. Martinez-Davalos, R. Nuñez, S. Popinet, and S. Zaleski, Phys. Rev. E **63**, 046309 (2001).
[8] J. Eggers, J. R. Lister, and H. A. Stone, J. Fluid Mech. **401**, 293 (1999).
[9] D. G. A. L. Aarts, H. N. W. Lekkerkerker, H. Guo, G. H. Wegdam, and D. Bonn, Phys. Rev. Lett. **95**, 164503 (2005).
[10] J. D. Paulsen, R. Carmigniani, A. Kannan, J. C. Burton, and S. R. Nagel, Nat. Commun. **5**, 3182 (2014).
[11] J. D. Paulsen, J. C. Burton, S. R. Nagel, S. Appathurai, M. T. Harris, and O. A. Basaran, Proc. Natl. Acad. Sci. USA **109**, 6857 (2012).
[12] J. E. Sprittles and Y. D. Shikhmurzaev, Phys. Fluids **24**, 122105 (2012).
[13] S. T. Thoroddsen, K. Takehara, and T. G. Etoh, J. Fluid Mech. **527**, 85 (2005).
[14] G. E. Charles and S. G. Mason, J. Colloid Sci. **15**, 236 (1960).
[15] G. E. Charles and S. G. Mason, J. Colloid Sci. **15**, 105 (1960).
[16] F. Blanchette and T. P. Bigioni, J. Fluid Mech. **620**, 333 (2009).
[17] F. Blanchette and T. P. Bigioni, Nat. Phys. **2**, 254 (2006).
[18] F. H. Zhang, E. Q. Li, and S. T. Thoroddsen, Phys. Rev. Lett. **102**, 104502 (2009).
[19] M. Garzon, D. Adalsteinsson, L. J. Gray, and J. A. Sethian, Interfaces Free Bound. **7**, 277 (2005).
[20] M. Garzon, L. J. Gray, and J. A. Sethian, J. Comput. Phys. **228**, 6079 (2009).
[21] M. Garzon, L. J. Gray, and J. A. Sethian, Phys. Rev. E **83**, 046318 (2011).
[22] M. Garzon, L. J. Gray, and J. A. Sethian, Int. J. Numer. Meth. Fluids **69**, 1124 (2012).
[23] M. Garzon, L. J. Gray, and J. A. Sethian, Phys. Rev. E **89**, 033011 (2014).
[24] A. Johansson, M. Garzon, and J. A. Sethian, J. Comput. Phys. **309**, 88 (2016).
[25] D. Adalsteinsson and J. A. Sethian, J. Comput. Phys. **148**, 2 (1999).
[26] J. A. Sethian, *Level Set Methods and Fast Marching Methods* (Cambridge University Press, Cambridge, UK, 1999).
[27] L. J. Gray, M. Garzon, V. Mantič, and E. Graciani, Int. J. Numer. Meth. Engrg. **66**, 2014 (2006).
[28] D. Leppinen and J. R. Lister, Phys. Fluids **15**, 568 (2003).
[29] See Supplemental Material at http://link.aps.org/supplemental/10.1103/PhysRevE.97.033112 for a movie of the merging process corresponding to mother droplet of radius $R_m = 0.15$, this coalescence pattern was classified as partial coalescence, second stage. A movie of the merging process corresponding to mother droplet of radius $R_m = 0.25$, this coalescence pattern was classified as partial coalescence, first stage. A movie of two equal drops coalescing under the action of an electrical field of intensity $E_\infty = 0.5$, after merging the unified droplet destabilizes and jet emission occurs at both droplet ends.
[30] G. Taylor, Proc. R. Soc. London, Ser. A **280**, 383 (1964).
[31] G. Taylor, Proc. R. Soc. London, Ser. A **313**, 453 (1969).
[32] R. T. Collins, J. J. Jones, M. T. Harris, and O. A. Basaran, Nat. Phys. **4**, 149 (2008).
[33] E. Giglio, B. Gervais, J. Rangama, B. Manil, B. A. Huber, D. Duft, R. Muller, T. Leisner, and C. Guet, Phys. Rev. E **77**, 036319 (2008).
[34] J. C. Burton and P. Taborek, Phys. Rev. Lett. **106**, 144501 (2011).
[35] C. Ferrera, J. M. López-Herrera, M. A. Herrada, J. M. Montanero, and A. J. Acero, Phys. Fluids **25**, 012104 (2013).
[36] S. Luo, J. Schiffbauer, and T. Luo, Phys. Chem. Chem. Phys. **18**, 29786 (2016).
[37] Z. Rozynek, A. Mikkelsen, P. Dommersnes, and J. O. Fossum, Nat. Commun. **5**, 3945 (2014).
[38] X. Chen, Y. Song, D. Li, and G. Hu, Phys. Rev. Appl. **4**, 024005 (2015).
[39] O. A. Basaran, T. W. Patzek, R. E. Benner, and L. E. Scriven, Ind. Eng. Chem. Res. **34**, 3454 (1995).